Inorganic Chemistry

Article

pubs.acs.org/IC

How Innocent are Potentially Redox Non-Innocent Ligands? Electronic Structure and Metal Oxidation States in Iron-PNN Complexes as a Representative Case Study

Burkhard Butschke,[†,⊥] Kathlyn L. Fillman,[§,⊥] Tatyana Bendikov,[‡] Linda J. W. Shimon,[‡] Yael Diskin-Posner,[‡] Gregory Leitus,[‡] Serge I. Gorelsky,[¶] Michael L. Neidig,*[,§] and David Milstein*[,†]

[†]Department of Organic Chemistry and [‡]Department of Chemical Research Support, The Weizmann Institute of Science, P.O. Box 26, 76100 Rehovot, Israel

[§]Department of Chemistry, University of Rochester, Rochester, New York 14627, United States

[¶]Centre for Catalysis Research and Innovation, University of Ottawa, Ottawa, Ontario K1N 6N5, Canada

Supporting Information

ABSTRACT: Herein we present a series of new α-iminopyridine-based iron-PNN pincer complexes [$FeBr_2L_{PNN}$] (**1**), [$Fe(CO)_2L_{PNN}$] (**2**), [$Fe(CO)_2L_{PNN}$](BF_4) (**3**), [Fe(F)-$(CO)_2L_{PNN}$](BF_4) (**4**), and [Fe(H)$(CO)_2L_{PNN}$](BF_4) (**5**) with formal oxidation states ranging from Fe(0) to Fe(II) (L_{PNN} = 2-[(di-*tert*-butylphosphino)methyl]-6-[1-(2,4,6-mesitylimino)ethyl]pyridine). The complexes were characterized by a variety of methods including ^{1}H, ^{13}C, ^{15}N, and ^{31}P NMR, IR, Mössbauer, and X-ray photoelectron spectroscopy (XPS) as well as electron paramagnetic resonance (EPR) and magnetic circular dichroism (MCD) spectroscopy, SQUID magnetometry, and X-ray crystallography, focusing on the assignment of the metal oxidation states. Ligand structural features suggest that the α-iminopyridine ligand behaves as a redox non-innocent ligand in some of these complexes, particularly in [$Fe(CO)_2L_{PNN}$] (**2**), in which it appears to adopt the monoanionic form. In addition, the NMR spectroscopic features (^{13}C, ^{15}N) indicate the accumulation of charge density on parts of the ligand for **2**. However, a combination of spectroscopic measurements that more directly probe the iron oxidation state (e.g., XPS), density functional theory (DFT) calculations, and electronic absorption studies combined with time-dependent DFT calculations support the description of the metal atom in **2** as Fe(0). We conclude from our studies that ligand structural features, while useful in many assignments of ligand redox non-innocence, may not always accurately reflect the ligand charge state and, hence, the metal oxidation state. For complex **2**, the ligand structural changes are interpreted in terms of strong back-donation from the metal center to the ligand as opposed to electron transfer.

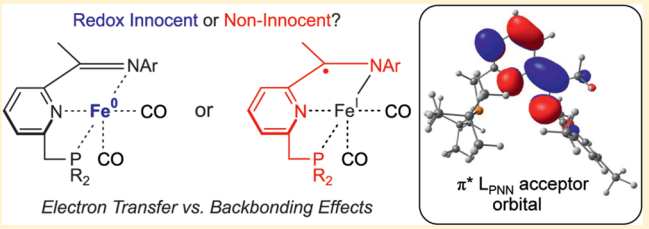

1. INTRODUCTION

It is the coordination chemist's desire to classify metal complexes in terms of their metal oxidation state. On the basis of this designation, reactivity patterns and the tendency of the metal center to bind certain ligands can be predicted. However, the assignment of metal oxidation states is often ambiguous, and the determination of the true electronic ground state of organometallic complexes can be challenging. For example, with the iron complex $[Fe(CO)_3(NO)]^-$ it took more than 50 years after its first synthesis to determine that this complex is not isoelectronic to $[Fe(CO)_4]^{2-}$, the latter of which is an Fe(−II) complex.[1] $[Fe(CO)_3(NO)]^-$ is rather an Fe(0) complex that contains an anionic NO^- ligand even though the linear coordination of the ligand to the metal center seemingly points to the presence of an NO^+ ligand.[1] Only a thorough spectroscopic analysis combined with density functional theory (DFT) and complete active space self-consistent field (CASSCF) calculations revealed the unexpected electronic structure of this iron complex. The challenge in the assignment of the metal oxidation state in this example is the *redox non-innocent nature* of the NO ligand, which can adopt charge states from −2 to +1.[2] In general, the determination of a metal oxidation state becomes ambiguous when redox non-innocent ligands are involved, and typical examples of such ligands are 1,2-dioxolenes (or catecholates),[3−5] 1,2-dithiolenes,[6] 2-amidophenoxides,[3,7−9] 2,2′-bipyridines,[10−16] α-iminopyridines,[17−19] 2,6-diiminopyridines,[20−26] and numerous others.[27−33] These ligands are able to change their redox state and to participate in electron transfer to or from the metal center; as a consequence, unfavorable metal oxidation states can be avoided or seemingly unusual metal oxidation states can be stabilized. In the past decade, catalysis research has made significant progress in utilizing the electronic flexibility possible with these ligands.[29,30,34−36] While the concept of *formal oxidation states*[37] is a formalism that relies on counting covalent bonds and ionic charges, a ligand set around a metal atom influences the electron density at the metal center when compared with the

Received: March 4, 2015
Published: April 28, 2015

DOI: 10.1021/acs.inorgchem.5b00509
Inorg. Chem. 2015, 54, 4909−4926

bare metal atom or ion. Consequently, it makes sense to think about electronic structure descriptors that will pave the way to a correct interpretation of physical and chemical properties of a given complex. One of these electronic-structure descriptors can be a parameter that reflects the *electron density distribution* at and around a metal center in a complex as a consequence of metal-ligation electronic interactions and, thus, the shift of electron density between the different fragments of the complex. Such a parameter is analogous to the oxidation state except that it is more closely connected to the physical picture (actual electronic distribution and metal−ligand interactions). Thus, it can be called a *physical oxidation state*. Redox non-innocent ligands can have a significant influence on the metal center, but examples also exist where they serve as innocent spectator ligands.[30] The actual mode of interaction of the ligand with the metal center is determined by the identity of the metal center, the actual ligand set, and sometimes even by second-sphere effects (counterions and interactions with solvent molecules).[38] To determine if a ligand participates in electron transfer to or from the metal center (and, hence, if it is redox non-innocent in the complex), its geometry within a given metal complex can be used as a criterion, and this correlation of the ligand geometry with its charge state is based on a variety of thorough studies.[9−13,15−19,21,22,24−26,39] The term *metrical [ligand] oxidation states* was coined in this context.[3] This approach is very reasonable since electron transfer to or from a ligand leads to structural changes within the ligand. However, ligand structural changes could also be the consequence of back-donation from the metal to the ligand as evidenced by a recent computational study where it was shown that both effects (electron transfer and backbonding) would indistinguishably cause the same type of ligand structural changes.[40,41] Backbonding, however, which serves as the classical explanation for geometric changes of various ligands such as CO or C_2H_4 upon binding to a metal center, would not be expected to result in changes of the metal oxidation state. While structural changes associated with classical backbonding are continuous, rather discrete ligand structural changes would be expected for integer electron transfer; and indeed, in studies concerning redox non-innocent ligands, stepwise changes of the ligand structure are usually described, which lead to characteristic bond lengths independent of the metal center involved.[3,9,15,18] Ultimately, it is this concept of stepwise ligand structural changes with the ligand oxidation state that provides the basis for the use of ligand geometries as a measure for the ligand charge state. On the other hand, there are examples in which the structural features of redox non-innocent ligands appear intermediate between the discretely charged forms, and this observation is usually explained in terms of delocalization phenomena.[18] No matter how ligand structural features are interpreted, in terms of backbonding or as a consequence of electron transfer, one must keep in mind that these interpretations are fundamentally distinct since backbonding is continuous, whereas electron transfer in these systems is described in terms of integer behavior. Thus, the concept of a physical oxidation state of a metal center appears attractive and can be helpful in descriptions of the electronic structure. Since such electronic-structure parameters are not physically observable, they cannot be probed by a single physical/spectroscopic method. Rather, only a multitechnique approach allows a comprehensive understanding of a given complex and provides means to determine the most suitable description of the electronic structure.

A particularly challenging system for the identification of the metal oxidation state is the 2,6-diiminopyridine-based iron dicarbonyl complex $[Fe(CO)_2L_{NNN}]$ depicted in Figure 1a.[24,42,43] The structural features of this formal Fe(0) complex

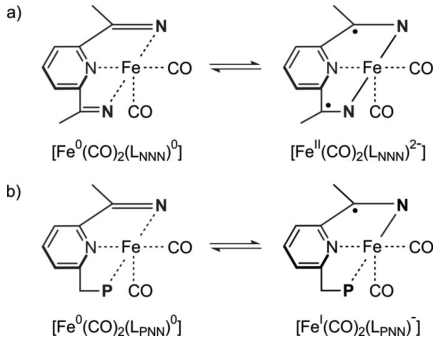

Figure 1. Illustration of the concept of *redox non-innocent* ligands: (a) two formulations for a 2,6-bisiminopyridine-based $[Fe(CO)_2L_{NNN}]$ complex (N = NAr) as reported earlier[24,42] and (b) possible formulations for an α-iminopyridine-based $[Fe(CO)_2L_{PNN}]$ complex (N = NAr, P = PR_2) as discussed in this study.

indicate the presence of a dianionic NNN ligand,[24] which would make this complex an Fe(II) system. The spectroscopic features and broken-symmetry (BS) calculations, however, do not unequivocally support an Fe(II) assignment, and an Fe(0) formulation was also considered possible.[24] An α-iminopyridine-based iron-PNN dicarbonyl complex such as $[Fe(CO)_2L_{PNN}]$ (Figure 1b) would presumably suffer from the same dilemma concerning the oxidation-state assignment, though Fe(0) and Fe(I) would be the anticipated limiting oxidation states. A comparison of the spectroscopic features of both types of complexes should provide insight toward the actual physical oxidation states present.

Herein, we present the synthesis and characterization of a series of α-iminopyridine-based iron-PNN pincer complexes $[FeBr_2L_{PNN}]$ (**1**), $[Fe(CO)_2L_{PNN}]$ (**2**), $[Fe(CO)_2L_{PNN}](BF_4)$ (**3**), $[Fe(F)(CO)_2L_{PNN}](BF_4)$ (**4**), and $[Fe(H)(CO)_2L_{PNN}](BF_4)$ (**5**), which cover formal oxidation states of 0 to +2 (L_{PNN} = 2-[(di-*tert*-butylphosphino)methyl]-6-[1-(2,4,6-mesitylimino)ethyl]pyridine, see Figure 2).[44] All complexes are characterized by means of a variety of spectroscopic techniques and other methods including ^1H, ^{13}C, ^{15}N, and ^{31}P NMR spectroscopy, IR, Mössbauer and X-ray photoelectron spectroscopy (XPS), electron paramagnetic resonance (EPR), and magnetic circular dichroism (MCD) spectroscopy, as well as SQUID magnetometry, cyclic voltammetry (CV), and X-ray crystallography. Density functional theory (DFT) calculations are employed to investigate the electronic structure of the complexes in further detail. Also, the 2,6-bisiminopyridine-based complexes $[FeBr_2L_{NNN}]$ (**6**) and $[Fe(CO)_2L_{NNN}]$ (**7**) were synthesized and characterized for this study (L_{NNN} = 2,6-bis-[1-(mesitylimino)ethyl]pyridine, see Figure 2). While metal oxidation state assignments in these complexes based on ligand metrical parameters would suggest redox non-innocent ligand behavior, we demonstrate that detailed electronic-structure studies combining multiple spectroscopic methods (i.e., Mössbauer, EPR, MCD, XPS, electronic absorption spectroscopy) complemented by DFT and time-dependent DFT (TD-DFT) studies support the presence of redox-innocent ligands. Overall, these studies demonstrate the importance of a multitechnique approach in elucidating the electronic structure

DOI: 10.1021/acs.inorgchem.5b00509
Inorg. Chem. 2015, 54, 4909−4926

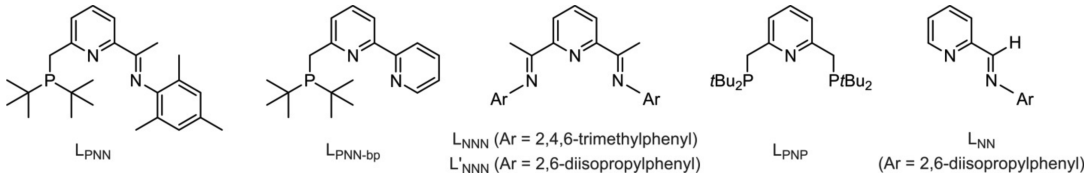

Figure 2. Overview of the PNN, NNN, PNP, and NN ligands discussed in this study.

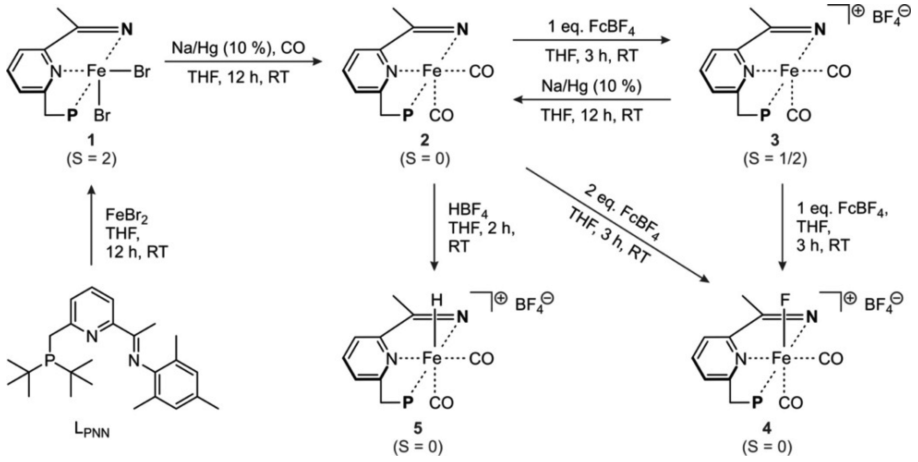

Figure 3. Overview of the iron complexes $[FeBr_2L_{PNN}]$ (**1**), $[Fe(CO)_2L_{PNN}]$ (**2**), $[Fe(CO)_2L_{PNN}](BF_4)$ (**3**), $[Fe(F)(CO)_2L_{PNN}](BF_4)$ (**4**), and $[Fe(H)(CO)_2L_{PNN}](BF_4)$ (**5**) as synthesized starting from the new PNN ligand L_{PNN} (N = NMes (Mes = 2,4,6-trimethyl phenyl), P = P^{t}Bu$_2$).

in complexes of potentially redox non-innocent ligands as well as the contributions of backbonding effects in such complexes.

2. RESULTS AND ANALYSIS

2.1. $[FeBr_2L_{PNN}]$ (1). The blue, paramagnetic iron PNN complex $[FeBr_2L_{PNN}]$ (**1**) is synthesized by the reaction of L_{PNN} with anhydrous $FeBr_2$ in tetrahydrofuran (THF) at room temperature, and this complex serves as a starting point for the syntheses of complexes **2**−**5** (Figure 3).

Crystals of suitable quality for X-ray diffraction were grown from a benzene solution of **1** at room temperature (Figure 4A). The Fe−N1 and Fe−N2 distances of 2.208(2) and 2.171(2) (see Table 1), respectively, are characteristic for a high-spin (hs) complex,[45,46] and the magnetic-moment measurements confirm this assignment (Evans' method:[47] μ_{eff} = 5.4 (at 298 K); SQUID: μ_{eff} = 4.77 (at 298 K, see Supporting Information for further details)).

For α-iminopyridine complexes, Wieghardt and co-workers described the C═N, C_{imine}−C_{ipso}, and C_{ipso}−N_{py} bond lengths to be indicative of the ligand charge state, and values of 1.28, 1.47, and 1.35 Å, respectively, were reported to be characteristic for the neutral form.[17−19] For $[FeBr_2L_{PNN}]$ (**1**) we found values of 1.282(4), 1.488(5), and 1.348(4) Å (see Table 1), respectively, which are well in agreement with a neutral formulation. Consequently, $[FeBr_2L_{PNN}]$ (**1**) is a hs-Fe(II) complex. This assignment is fully in agreement with the Mössbauer spectrum of **1** at 80 K, which is well-fit as a doublet with parameters of δ = 0.94 mm s^{-1}, ΔE_Q = 2.59 mm s^{-1} (Figure 4 and Table 2).[48] Moreover, saturation magnetization data collected at 8810 cm^{-1} (Figure 4C, inset) are well-described by an S = 2 negative zero-field split ground state model with ground state spin Hamiltonian parameters of δ = 1.4 ± 0.1 cm^{-1} and $g_{\|}$ = 9.0 ± 0.2, corresponding to the ligand-field parameters Δ = −1400 ± 200 cm^{-1} and $|V/2\Delta|$ = 0.18 ± 0.02 (where $\Delta = E(d_{xz,yz}) - E(d_{xy})$ and $V = E(d_{xz}) - E(d_{yz})$).

In addition, we employed XPS for the characterization of the electron density at the metal center, which is related to the *physical metal oxidation state*. XPS, as well as electron-spectroscopic methods in general, has the advantage of being applicable for any element (except hydrogen), in any possible electronic state (in contrast to NMR or Mössbauer spectroscopy, which are available only for a limited set of elements and spin states). Several decades ago, this technique was applied for the characterization of a wide range of organometallic complexes and materials including iron-containing species,[49−54] while it was within the past decade only sparsely used for organometallic compounds.[40,55,56] Certain spectral features, so-called shake-up lines,[49,51] also allow for the distinction of diamagnetic and paramagnetic compounds (see Supporting Information for details). With respect to the determination of metal oxidation states using XPS, it is independently reported that, irrespective of the metal, a formal oxidation-state change of one is accompanied by a change in the electron binding energy of ∼1 eV[50] (or 1.2 eV[57]). Note, however, that this value is merely empirical and that it applies only if the ligand sets are comparable. For $[FeBr_2L_{PNN}]$ (**1**), the maximum of the Fe $2p_{3/2}$ peak in the XPS spectrum is located at a binding energy of 709.4 eV (entry 1 in Table 3), and the comparison with the corresponding chloro complex $[FeCl_2L_{PNN}]$ (**1′**) (709.4 eV, entry 2 in Table 3) indicates that the electronic influence of Br versus Cl ligands on the Fe center is comparable. This behavior is expected and in agreement with previous studies.[50]

However, in the series $[FeBr_2L_{NNN}]$ (**6**), $[FeBr_2L_{PNN}]$ (**1**), and $[FeBr_2L_{PNP}]$ (Table 3, entries 3, 1, and 4, respectively; for the ligands, see Figure 2), in which the imine arms of $[FeBr_2L_{NNN}]$ (**6**) are successively exchanged for phosphine donors, a systematic decrease of the Fe $2p_{3/2}$ binding energies by 0.6 eV in 0.3 eV steps is observed. This finding is in agreement with the stronger electron-donating ability of phosphines when compared with imine ligands, and XPS is

DOI: 10.1021/acs.inorgchem.5b00509
Inorg. Chem. 2015, 54, 4909−4926

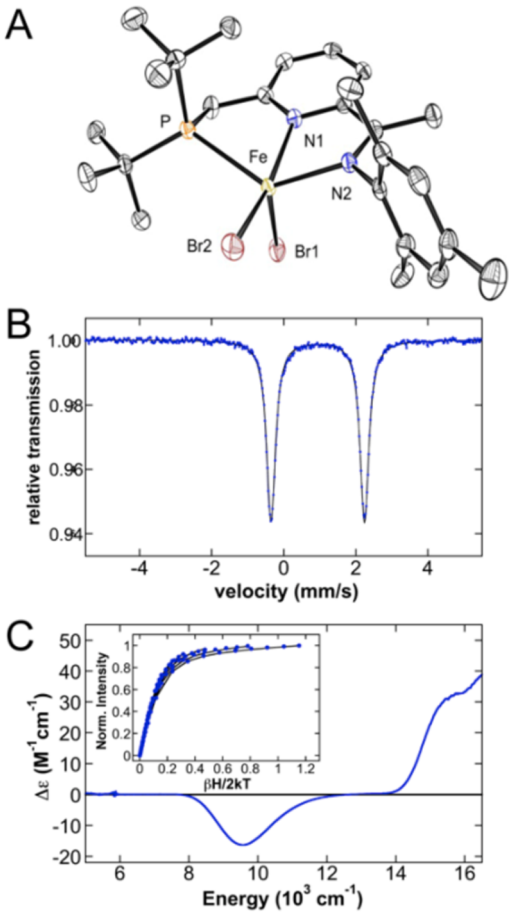

Figure 4. Structural and spectroscopic characterization of $[FeBr_2L_{PNN}]$ (**1**). (A) X-ray molecular structure of **1** with 50% probability thermal ellipsoids; the hydrogen atoms and a cocrystallized benzene molecule are omitted for clarity; selected bond lengths are given in Table 1. (B) 80 K Mössbauer spectrum of **1**. (C) 5 K, 7 T NIR MCD spectrum of **1**. (inset) Saturation-magnetization data (dots) and best fit (lines) collected at 8810 cm^{-1}.

sensitive to this effect. Note, however, that this observation also demonstrates the difference between a formal and a physical oxidation state: while the former adopts integer values by definition (and all three dibromide complexes under discussion are formal Fe(II) complexes),[37] the latter is continuous.

Spin-unrestricted DFT calculations were used to further evaluate the electronic structure of $[FeBr_2L_{PNN}]$ (**1**). Geometry optimization at the PBEPBE/TZVP level yielded overall structural features, bond lengths, and angles in good agreement with those observed by crystallography with only some minor bond elongations and contractions of the metal−ligand bonds, particularly the Fe−L_{PNN} bonds (solvent model). The optimized structure of **1** is best described as a distorted square pyramidal complex with Fe−P, Fe−N1, and Fe−N2 bond lengths of 2.591, 2.151, and 2.103 Å, respectively, Fe−Br bond

Table 2. Summary of the 80 K ^{57}Fe Mössbauer Parameters for Iron L_{PNN} Complexes

complex	δ in mm s^{-1}	ΔE_Q in mm s^{-1}
$[FeBr_2L_{PNN}]$ (**1**)	0.94	2.59
$[Fe(CO)_2L_{PNN}]$ (**2**)	0.00	1.14
$[Fe(CO)_2L_{PNN}](BF_4)$ (**3**)	0.12	0.54
$[Fe(F)(CO)_2L_{PNN}](BF_4)$ (**4**)	0.04	0.55
$[Fe(H)(CO)_2L_{PNN}](BF_4)$ (**5**)	−0.04	1.48

Table 3. Fe $2p_{3/2}$ Electron Binding Energies for the Iron Complexes Discussed in This Study

entry	complex	Fe $2p_{3/2}$ BE[a] in eV
1	$[FeBr_2L_{PNN}]$ (**1**)	709.4
2	$[FeCl_2L_{PNN}]$ (**1′**)	709.4
3	$[FeBr_2L_{NNN}]$ (**6**)	709.7
4	$[FeBr_2L_{PNP}]^b$	709.1
5	$[Fe(CO)_2L_{PNN}]$ (**2**)	708.1
6	$[Fe(CO)_2L_{NNN}]$ (**7**)	708.4
7	$[FeBr_2L_{PNN\text{-}bp}]^c$	709.5
8	$[Fe(CO)_2L_{PNN\text{-}bp}]^c$	708.0
9	$[Fe(CO)_2L_{PNN}](BF_4)$ (**3**)	708.8
10	$[Fe(F)(CO)_2L_{PNN}](BF_4)$ (**4**)	709.9
11	$[Fe(H)(CO)_2L_{PNN}](BF_4)$ (**5**)	709.2

[a]Measured by XPS. [b]Prepared according to ref 58. [c]Data taken from ref 40.

Table 1. Selected Bond Lengths [Å] of $[FeBr_2L_{PNN}]$ (1), $[Fe(CO)_2L_{PNN}]$ (2), $[Fe(CO)_2L_{PNN}](BF_4)$ (3), $[Fe(F)(CO)_2L_{PNN}](BF_4)$ (4), and $[Fe(H)(CO)_2L_{PNN}](BF_4)$ (5)

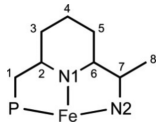

	1	2	3	4	5
Fe−N1	2.208(2)	1.924(2)	1.974(3)	1.957(3)	1.967(1)
Fe−N2	2.171(2)	1.919(2)	1.990(4)	2.008(3)	1.985(1)
Fe−P	2.5147(8)	2.2231(6)	2.259(1)	2.293(1)	2.2329(6)
P−C1	1.833(4)	1.847(2)	1.837(4)	1.838(4)	1.845(2)
C1−C2	1.508(5)	1.491(3)	1.498(6)	1.489(6)	1.500(2)
C2−C3	1.393(5)	1.366(3)	1.394(5)	1.398(6)	1.397(2)
C3−C4	1.381(5)	1.404(3)	1.374(6)	1.370(6)	1.386(2)
C4−C5	1.389(5)	1.363(3)	1.388(6)	1.382(6)	1.393(2)
C5−C6	1.385(4)	1.411(3)	1.389(5)	1.382(6)	1.386(2)
C6−N1 (C_{ipso}−N_{py})	1.348(4)	1.377(3)	1.361(5)	1.360(5)	1.357(2)
C6−C7 (C_{imine}−C_{ipso})	1.488(5)	1.410(3)	1.452(6)	1.468(6)	1.469(2)
C7−N2 (C═N)	1.282(4)	1.339(3)	1.299(5)	1.295(5)	1.293(2)

DOI: 10.1021/acs.inorgchem.5b00509
Inorg. Chem. 2015, 54, 4909−4926

lengths of 2.458 and 2.483 Å, an N1−Fe−N2 bond angle of 75.38°, and an N1−Fe−P bond angle of 75.23° (compare with the crystal details given in Figure 4A and Table 1). The molecular orbitals and their corresponding energies as well as excitation energies were calculated from the optimized structure at the B3LYP/TZVP level. Importantly, TD-DFT calculations provide excellent agreement between calculated and experimentally determined d−d and charge-transfer (CT) transitions (from MCD and UV−vis spectra), providing further validation of the quality of the DFT model (see Supporting Information for details). Both the experimental and computational studies of **1** are indicative of a hs-Fe(II) complex (S = 2). A molecular orbital energy diagram for **1** is given in the Supporting Information.

2.2. [Fe(CO)$_2$L$_{PNN}$] (2). Reduction of the Fe(II) dibromide complex [FeBr$_2$L$_{PNN}$] (**1**) with an excess of sodium amalgam (10%) under a CO atmosphere at room temperature gives rise to [Fe(CO)$_2$L$_{PNN}$] (**2**). This formally Fe(0) complex is obtained as an intensely purple, diamagnetic solid, which is well-soluble in all common solvents including pentane, and crystals were grown from a saturated pentane solution at −35 °C (Figure 5).

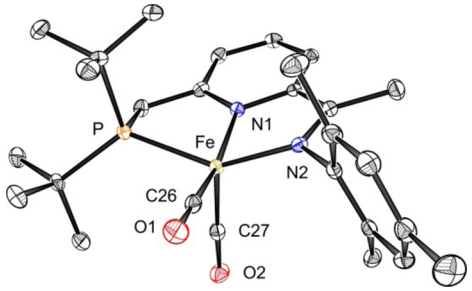

Figure 5. Molecular structure of [Fe(CO)$_2$L$_{PNN}$] (**2**) with 50% probability thermal ellipsoids. The hydrogen atoms and a cocrystallized pentane molecule are omitted for clarity. Selected bond lengths are given in Table 1.

The crystal structure of **2** indicates a distorted square pyramidal coordination sphere around the Fe center (OC−Fe−CO = 96.89(9)°, N$_{py}$−Fe−CO = 100.75(8)° and 162.34(8)°). Also, the IR spectra in both the solid state and in solution confirm an ∼90° angle between the two CO ligands as two absorptions in a 1:1 intensity ratio are observed (see Table 4).

However, in the NMR spectra recorded at room temperature, [Fe(CO)$_2$L$_{PNN}$] (**2**) appears C_{2v} symmetric with a plane of symmetry defined by the pyridine ring: in the ^{1}H NMR spectrum only one doublet is observed for the ^{t}Bu groups at 0.98 ppm (d, 18H, $^3J_{HP}$ = 12.6 Hz), the methylene group at 3.27 ppm (d, 2H, $^2J_{HP}$ = 8.3 Hz), and the *o*-methyl and the *m*-hydrogen atoms of the mesityl group at 2.25 ppm (s, 6H) and 6.95 ppm (s, 2H), respectively. For the CO ligands, only one doublet is observed at 221.1 ppm (d, $^2J_{CP}$ = 11.3 Hz) in the ^{13}C NMR spectrum. Similar discrepancies in the structural assignment upon comparison of the crystal structure and NMR data have been observed for iron-dicarbonyl complexes before.[24,40,59] The C=N, C$_{imine}$−C$_{ipso}$, and C$_{ipso}$−N$_{py}$ bond lengths determined for [Fe(CO)$_2$L$_{PNN}$] (**2**) (1.339(3), 1.410(3), and 1.377(3) Å, respectively; see Table 1) are very similar to those reported for the monoanionic form of α-iminopyridine ligands according to Wieghardt and co-workers, that is, 1.34, 1.41, and 1.39 Å, respectively.[17−19] On the basis of the ligand structural data alone, [Fe(CO)$_2$L$_{PNN}$] (**2**) would be assigned as an Fe(I) complex. According to Figure 1b, electron transfer to the PNN ligand should give rise to a special signature with respect to the imine carbon atom C7 as well as to the imine nitrogen atom N2. While for the free PNN ligand the imine carbon atom C7 exhibits the highest ^{13}C chemical shift among the quaternary carbon atoms C2, C6, and C7 (and even overall), in [Fe(CO)$_2$L$_{PNN}$] (**2**), the ^{13}C NMR resonance of C7 is shifted particularly to higher field when compared with C2 and C6 (see Table 5).

Table 4. Infrared Stretches ν_{CO} for Complexes [Fe(CO)$_2$L$_{PNN}$] (2), [Fe(CO)$_2$L$_{PNN}$](BF$_4$) (3), [Fe(F)(CO)$_2$L$_{PNN}$](BF$_4$) (4), [Fe(H)(CO)$_2$L$_{PNN}$](BF$_4$) (5), and [Fe(CO)$_2$L$_{NNN}$] (7) as Determined in the Solid State on NaCl Plates

	2[a]	3	4	5	7
ν(CO$_{sym}$) [cm^{-1}]	1934 (1952)	1987	2052	2022	1949
ν(CO$_{asym}$) [cm^{-1}]	1875 (1897)	1922	2015	1973	1878
ν(Fe−H) [cm^{-1}]				1929	

[a]Values in parentheses were determined in a pentane solution.

Table 5. Selected NMR Spectroscopic Data of the Free PNN Ligand as well as the Complexes [Fe(CO)$_2$L$_{PNN}$] (2), [Fe(F)(CO)$_2$L$_{PNN}$](BF$_4$) (4), and [Fe(H)(CO)$_2$L$_{PNN}$](BF$_4$) (5)

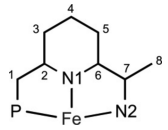

	PNN ligand[a]	2[a]	4[a]	5[a]
δ(P) [ppm]	38.5 (s)	138.4 (s)	120.3 (s)	106.9 (d, $^2J_{PF}$ = 9.7 Hz)
δ(N1) [ppm]	311.5 (s)	258.1 (s)	258.6 (s)	257.6 (s)
δ(N2) [ppm]	334.0 (s)	259.2 (s)	274.8 (s)	274.1 (s)
δ(C2) [ppm]	161.2 (d, $^2J_{CP}$ = 14.1 Hz)	159.2 (d, $^2J_{CP}$ = 7.8 Hz)	162.4 (d, $^2J_{CP}$ = 4.0 Hz)	164.5 (d, $^2J_{CP}$ = 2.8 Hz)
δ(C6) [ppm]	155.8 (s)	144.7 (d, $^3J_{CP}$ = 5.1 Hz)	153.9 (d, $^3J_{CP}$ = 4.3 Hz)	156.6 (d, $^3J_{CP}$ = 3.5 Hz)
δ(C7) [ppm]	168.0 (s)	144.9 (s)	173.3 (s)	179.9 (s)

[a]The ^{15}N NMR chemical shifts were determined by ^{15}N−^{1}H HMQC experiments.

This observation might be in line with an accumulation of charge density on this site as would be expected according to Figure 1b. The ^{15}N NMR chemical shift of N2 (when compared with those obtained for [Fe(F)(CO)$_2$L$_{PNN}$](BF$_4$) (**4**) and [Fe(H)(CO)$_2$L$_{PNN}$](BF$_4$) (**5**), vide infra) is also in line with this interpretation, and we will come back to this aspect further below. Moreover, according to the crystal structure data of [Fe(CO)$_2$L$_{PNN}$] (**2**), the pyridine ring shows alternating bond lengths (compare the C−C bonds connecting C2−C6 in Table 1). Even though such a behavior would rather be expected for the dianionic form of an α-iminopyridine ligand,[17−19] this observation is in line with the shift of electron density from the metal center to the ligand.

In contrast to the NMR and crystal structure data, which suggest an Fe(I) description of [Fe(CO)$_2$L$_{PNN}$] (**2**) but which reflect only the ligand properties in a direct fashion, the

DOI: 10.1021/acs.inorgchem.5b00509
Inorg. Chem. 2015, 54, 4909−4926

Mössbauer data (δ = 0.00 mm s^{-1}, ΔE_Q = 1.14 mm s^{-1}, Table 2) for this complex are not unequivocally in agreement with an Fe(I) designation, since an assignment as either Fe(0) or ls-Fe(II) (ls = low spin) is possible based on the parameters, demonstrating the challenge in correlating metal oxidation states with Mössbauer parameters in low-valent iron complexes.[48] Note that very similar parameters (δ = 0.03 mm s^{-1}, ΔE_Q = 1.17 mm s^{-1}) were found for Chirik's 2,6-bisiminopyridine-based complex [Fe(CO)$_2$L'$_{NNN}$], for which both an Fe(0) and a ls-Fe(II) formulation was considered possible.[24] In Chirik's study, the Fe(II) interpretation was suggested by the ligand structural features, which were interpreted as being indicative of a dianionic ligand, while the Fe(0) assignment was based on the Mössbauer data. Also broken-symmetry DFT calculations did not provide a more conclusive picture, and the authors concluded later that "the electronic structure can be considered a hybrid of the Fe(0) and Fe(II) limiting resonance forms."[42]

XPS measurements on [Fe(CO)$_2$L$_{PNN}$] (**2**) give rise to an Fe 2p$_{3/2}$ binding energy of 708.1 eV (entry 5 in Table 3), which is 1.3 eV lower than for the formal Fe(II) dibromide complex [FeBr$_2$L$_{PNN}$] (**1**) (entry 1 in Table 3). Thus, the electron density on the iron center of [Fe(CO)$_2$L$_{PNN}$] (**2**) appears considerably increased when compared with that of [FeBr$_2$L$_{PNN}$] (**1**). The same binding energy difference is found for the couple [FeBr$_2$L$_{NNN}$] (**6**)/[Fe(CO)$_2$L$_{NNN}$] (**7**) (entries 3 and 6 in Table 3), and consequently, the iron centers in both [Fe(CO)$_2$L$_{PNN}$] (**2**) and [Fe(CO)$_2$L$_{NNN}$] (**7**) look very similar electronically. Note that the Fe 2p$_{3/2}$ binding-energy values determined in this study for [FeBr$_2$L$_{PNN}$] (**1**) and [Fe(CO)$_2$L$_{PNN}$] (**2**) very much resemble those obtained earlier in an independent investigation from our group, in which the bipy-analogous PNN pincer complexes [FeBr$_2$L$_{PNN\text{-}bp}$] and [Fe(CO)$_2$L$_{PNN\text{-}bp}$] were investigated (entries 7 and 8 in Table 3; for the ligand see Figure 2; bipy = 2,2′-bipyridine).[40] Thus, all three iron-dicarbonyl complexes [Fe(CO)$_2$L$_{PNN}$] (**2**), [Fe(CO)$_2$L$_{NNN}$] (**7**), and [Fe(CO)$_2$L$_{PNN\text{-}bp}$] appear to be electronically very similar based on the XPS data, while the crystal structures of these complexes indicate oxidation states of Fe(I) for the PNN complexes[40] and Fe(II) for the NNN complex.[24]

To further evaluate the electronic structure of complex **2**, DFT studies were performed. Initial geometry optimization at the PBEPBE/TZVP level yielded overall structural features, bond lengths, and angles in good agreement with those observed by crystallography. The optimized structure of **2** is best described as a distorted square pyramidal complex with Fe−P, Fe−N1, and Fe−N2 bond lengths of 2.258, 1.944, and 1.931 Å, respectively, Fe−CO bond lengths of 1.751 and 1.756 Å, an N1−Fe−N2 bond angle of 79.80°, and an N1−Fe−P bond angle of 82.26°. This optimized geometry correlates well with the crystal structure (see Figure 5 and Table 1). Note also that the bond elongations and contractions of the N1−C6, C6−C7, and C7−N2 bonds seen in the crystal structure of **2** are reproduced in the calculated structure to within 0.015 Å (see Table 1). As previously discussed, according to the structural parameters complex **2** should be assigned as an Fe(I) complex. In addition, the XPS data seem to indicate that an Fe(I) situation might apply for **2** if the 1.3 eV difference in the electron binding energy compared with [FeBr$_2$L$_{PNN}$] (**1**) (see Table 3) is interpreted in terms of an oxidation state difference of one. However, it is important to recall that **1** carries two bromide ligands, while **2** contains two CO ligands, and such ligand changes have a strong influence on the apparent binding energy.[50] Therefore, to further analyze the electronic structure of **2**, spin-unrestricted BS calculations at the B3LYP/TZVP level were completed to test the possibility of L$_{PNN}$ acting as a redox-active ligand in this complex. Taking into account that **2** has a diamagnetic ground state (S = 0), three different computational models were explored (see Supporting Information for details): (i) the neutral-ligand description corresponding to [Fe^0(CO)$_2$(L$_{PNN}$)], (ii) the BS(1,1) approach to yield the electronic ground state of [Fe^I(CO)$_2$(L$_{PNN}^-$)] (considering the transfer of both an α- or a β-spin electron from Fe (now, S = 1/2) to L$_{PNN}$), and (iii) the BS(2,2) case, producing [Fe^{II}(CO)$_2$(L$_{PNN}^{2-}$)] (considering the transfer of two electrons from Fe to generate either S = 0 or S = 1 with the Fe site being antiferromagnetically coupled to L$_{PNN}^{2-}$ to give an S_{total} = 0 complex). Notably, the Fe^I/[L$_{PNN}^-$] models converged to the same result: a system with a nonzero spin density on Fe and an electronic energy that is 0.61 kcal/mol lower than for the Fe^0/[L$_{PNN}$] model, the latter of which converged to an electronic state with a zero spin density on the Fe atom. The Fe^{II}/[L$_{PNN}^{2-}$] models were found to depend on the iron spin state, and electron densities consistent with either the Fe^I/[L$_{PNN}^-$] or Fe^0/[L$_{PNN}$] electronic descriptions could be obtained. Importantly, however, previous computational studies of 2,2′-bipyridine complexes of iron, cobalt, vanadium, and titanium using a variety of exchange-correlation (XC) functionals have demonstrated that B3LYP, a hybrid XC functional, can yield unreliable results in BS calculations of pincer complexes of this type and that nonhybrid XC functionals (e.g., PBE, HCTC, BLYP) give more accurate predictions.[41] This previous study and the small energy differences between the two ground-state descriptions found in our B3LYP calculations motivated the evaluation of our three computational models across a series of XC functionals. Analogous calculations to those described using B3LYP were performed using BLYP, PBEPBE, HCTC, and M06L with the same basis set, TZVP, as before. Importantly, all calculations using these four XC functionals were found to converge to an electronic state with a zero atomic spin density on Fe, which is consistent with the [Fe^0(CO)$_2$(L$_{PNN}$)] description with no unpaired electrons on Fe or L$_{PNN}$.

Further support for the [Fe^0(CO)$_2$(L$_{PNN}$)] ground-state electronic structure description derives from TD-DFT calculations performed for **2** for both the Fe^0/[L$_{PNN}$] and Fe^I/[L$_{PNN}^-$] electronic descriptions (note: B3LYP models were utilized as both descriptions were obtained). Notably, the TD-DFT calculations for Fe^I/[L$_{PNN}^-$] predict an additional low-energy d−d transition at ∼8660 cm^{-1} compared to the Fe^0/[L$_{PNN}$] solution. Therefore, near-IR (NIR) absorption studies were completed for **2** (see Supporting Information for details) that showed no additional low-energy d−d transition at <10 000 cm^{-1} (even at very high complex concentrations). This experimental evidence is consistent with the assignment of **2** as a ls-Fe(0) complex with no unpaired electron on either Fe or L$_{PNN}$. While it is likely that the [Fe^0(CO)$_2$(L$_{PNN}$)] and [Fe^I(CO)$_2$(L$_{PNN}^-$)] electronic states are, in fact, relatively close in energy, the combined results of XPS, electronic absorption spectroscopy, and DFT/TD-DFT studies are more consistent with L$_{PNN}$ acting as a redox-innocent ligand in complex **2**.

Because of these findings, all further DFT calculations were completed using the [Fe^0(CO)$_2$(L$_{PNN}$)] electronic ground-state description. The ground-state wave function of **2** is described by the frontier molecular orbitals (FMOs), which are shown in

DOI: 10.1021/acs.inorgchem.5b00509
Inorg. Chem. 2015, 54, 4909−4926

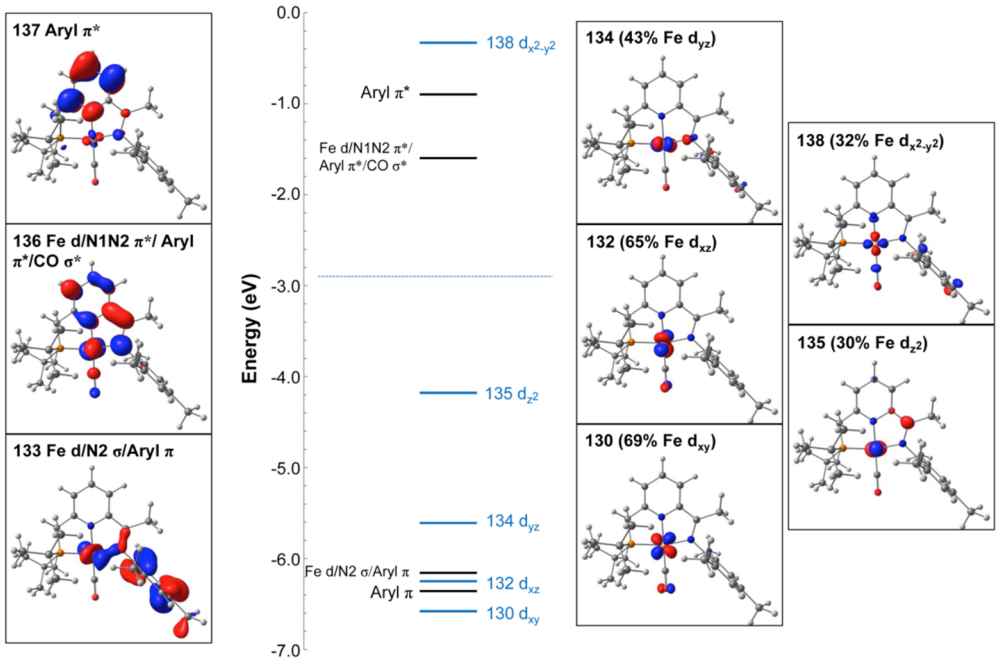

Figure 6. Calculated molecular orbital energy diagram for $[Fe(CO)_2L_{PNN}]$ (**2**).

Figure 6. The Fe d-orbitals are significantly mixed with CO and L_{PNN} character, and listed in order of increasing energy those are d_{xy}(130), d_{xz} (132), d_{yz} (134), d_{z^2} (135), and $d_{x^2-y^2}$ (138). In addition, there are FMOs that represent an occupied MO of Fe d-, N2 σ-, and aryl π-character (133), an unoccupied MO of Fe d-, N1N2 π^*-, aryl π^*-, and CO σ^*-character (136), and an unoccupied MO of aryl π^*-character (137).

TD-DFT calculations were also used to assign the observed transitions in the absorption spectrum (see Supporting Information for details). Overall, the energies of the absorption transitions correlate well to the TD-DFT calculated energies. However, the d−d and CT transitions are quite mixed, involving multiple L_{PNN}, CO, and Fe orbitals.

2.3. $[Fe(CO)_2L_{PNN}](BF_4)$ (3). Upon one-electron oxidation of $[Fe(CO)_2L_{PNN}]$ (**2**) with 1 equiv of ferrocenium tetrafluoroborate in THF at room temperature, $[Fe(CO)_2L_{PNN}](BF_4)$ (**3**) was isolated as a paramagnetic, green solid. Reduction of $[Fe(CO)_2L_{PNN}](BF_4)$ (**3**) with sodium amalgam (10%) in THF at room temperature gives rise to the regeneration of $[Fe(CO)_2L_{PNN}]$ (**2**) (Figure 3). This kind of reactivity has been indicated by the CV of $[Fe(CO)_2L_{PNN}]$ (**2**) (Figure 7a), which shows three redox processes between +1.0 and −3.5 V, and an analogous behavior was observed previously for a similar set of PNN-based iron−dicarbonyl pincer complexes.[40]

The waves at $E_{1/2}$ = −0.65 and −2.76 V are reversible as indicated by separate scans for these regions. We interpret these two waves in terms of one-electron oxidation and reduction processes relative to $[Fe(CO)_2L_{PNN}]$ (**2**) as reported by Chirik and co-workers for the NNN-iron dicarbonyl complex $[Fe(CO)_2L'_{NNN}]$.[42] The oxidation wave at +0.64 V, however, is not well-behaved reversible, and both reduction features at ca. 0.00 V and −1.48 V appear only if the cycling involves the oxidation at +0.64 V. While we have no chemical explanation for the two different reduction events, we speculate that the respective oxidation event involves the generation of dicationic $[Fe(CO)_2L_{PNN}]^{2+}$, which decomposes prior to electrochemical reduction. Higher scan rates of up to 600 mV s^{-1} do not make

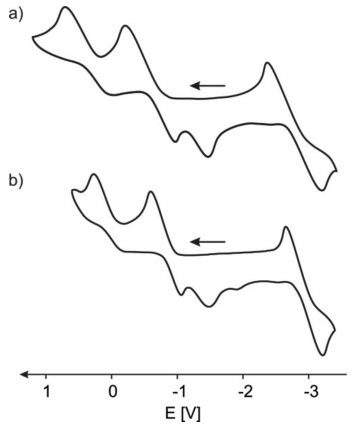

Figure 7. CVs of (a) $[Fe(CO)_2L_{PNN}]$ (**2**) and (b) $[Fe(CO)_2L_{PNN}](BF_4)$ (**3**) in THF (0.1 M $[^nBu_4N][BF_4]$ supporting electrolyte) at room temperature with scan rates of 100 mV s^{-1} (glassy-carbon working-electrode). Potentials are referenced relative to the Fc^+/Fc couple.

this process reversible. The fact, however, that the CVs of $[Fe(CO)_2L_{PNN}]$ (**2**) and $[Fe(CO)_2L_{PNN}](BF_4)$ (**3**) (Figure 7) exhibit similar features at comparable positions confirms the electrochemical formation of $[Fe(CO)_2L_{PNN}](BF_4)$ (**3**) during cyclic voltammetry of $[Fe(CO)_2L_{PNN}]$ (**2**). Complex **3** exhibits IR absorptions at 1922 and 1987 cm^{-1} in a 1:1 ratio, which are indicative of the presence of two CO ligands with an ∼90° angle between them. The higher wavenumbers compared with $[Fe(CO)_2L_{PNN}]$ (**2**) (see Table 4) are consistent with the reduction of electron density on the metal center upon one-electron oxidation, and the change of ca. 50 cm^{-1} is similar to that reported for the analogous NNN-ligated system described by Chirik and co-workers.[42] Further, the magnetic measurements (Evans' method: μ_{eff} = 2.1 (at 298 K); SQUID: μ_{eff} = 2.14 (at 298 K, see Supporting Information for further details)) are in agreement with a ls-Fe(I) assignment. The Mössbauer parameters of **3** at 80 K (δ = 0.12 mm s^{-1}, ΔE_Q = 0.54 mm s^{-1},

DOI: 10.1021/acs.inorgchem.5b00509
Inorg. Chem. 2015, 54, 4909−4926

Table 2)[48] are also similar to those reported by Chirik and coworkers for their $[Fe(CO)_2L'_{NNN}](BAr^F{}_4)$ complex, which was assigned as ls-Fe(I).[42] Further evidence for an Fe(I) assignment of **3** is provided by the Fe $2p_{3/2}$ binding energy of 708.8 eV (entry 9 in Table 3), as determined via XPS, which is 0.7 eV higher than of the parent compound $[Fe(CO)_2L_{PNN}]$ (**2**), the latter of which we assigned to be an Fe(0) complex. Single crystals of $[Fe(CO)_2L_{PNN}](BF_4)$ (**3**) were grown by diffusion of pentane into a THF solution at room temperature (Figure 8).

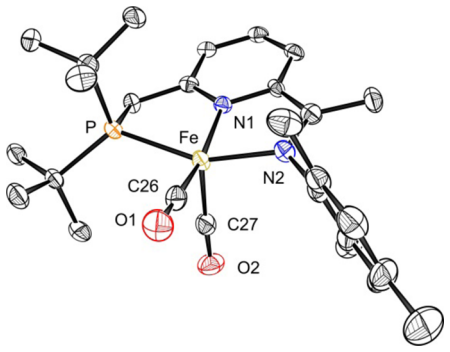

Figure 8. Molecular structure of $[Fe(CO)_2L_{PNN}](BF_4)$ (**3**) with 50% probability thermal ellipsoids. The hydrogen atoms, the BF_4^- counterion, and a cocrystallized THF molecule are omitted for clarity. Selected bond lengths are given in Table 1.

While the C═N, C_{imine}–C_{ipso}, and C_{ipso}–N_{py} parameters for $[FeBr_2L_{PNN}]$ (**1**) and $[Fe(CO)_2L_{PNN}]$ (**2**) are indicative of the presence of a neutral and a monoanionic α-iminopyridine ligand, respectively, for $[Fe(CO)_2L_{PNN}](BF_4)$ (**3**) the values are intermediate between the two descriptions (see Table 1). While other complexes are known in which only one α-iminopyridine ligand is bound to the metal center,[60−62] $[Fe(CO)_2L_{PNN}](BF_4)$ (**3**) is, to our knowledge, the first structurally characterized complex with a single α-iminopyridine ligand bound to the metal center, in which the structural parameters are between the neutral and the anionic description. Wieghardt and coworkers previously described an α-iminopyridine complex of iron, $[Fe(L_{NN})_2]^+$ (L = 2,6-diisopropyl-*N*-(pyridin-2-ylmethylene)aniline, Figure 2), in which the two bidentate NN ligands exhibit intermediate structural features.[18] This observation, however, was interpreted in terms of electron delocalization: the iron oxidation state in $[Fe(L_{NN})_2]^+$ was assigned to be Fe(II), while one negative charge was assumed to be distributed over the two L_{NN} ligands. Such an interpretation, however, can be clearly excluded for $[Fe(CO)_2L_{PNN}](BF_4)$ (**3**), which contains only one α-iminopyridine unit. While a critical reader might argue that the present PNN ligand is not a genuine α-iminopyridine ligand and that the additional phosphorus arm might be redox non-innocent itself, this option can be excluded since in all three complexes **1**, **2**, and **3**, both the P–C1 and the C1–C2 bond lengths are essentially unaltered (Table 1); the additional phosphorus donor thus acts as a mere spectator. The fact that in $[Fe(CO)_2L_{PNN}](BF_4)$ (**3**) the α-iminopyridine ligand adopts a geometry that is between those expected for a neutral and a monoanionic ligand rules out the possibility of the assignment of an integer charge state to the ligand and, thus, questions the strict interpretation of ligand structural changes in terms of electron-transfer processes. Rather, backbonding phenomena might account for this observation (vide infra).[41]

To further characterize the electronic structure of **3**, EPR and MCD spectroscopy were utilized. The 10 K EPR spectrum of **3** shown in Figure 9A clearly depicts a rhombic $g \approx 2$ signal (S =

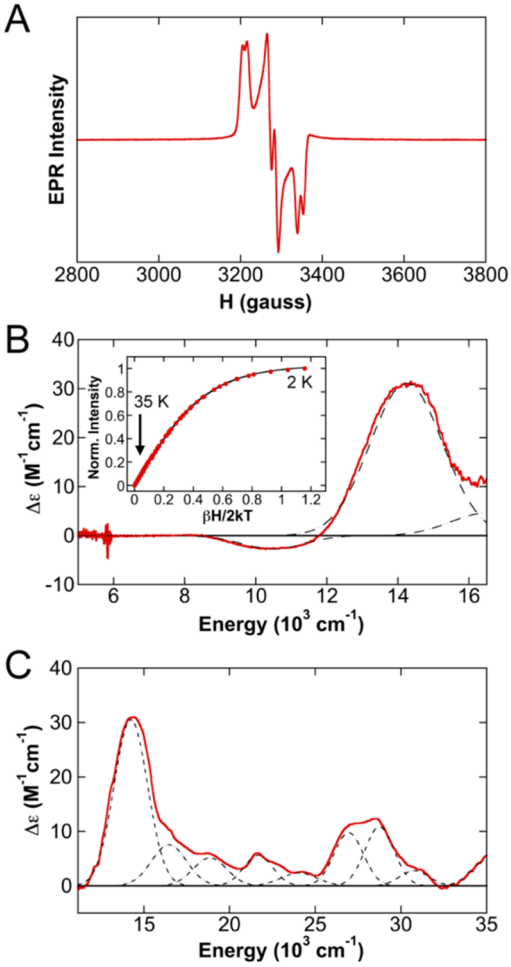

Figure 9. EPR and MCD spectroscopic characterization of $[Fe(CO)_2L_{PNN}](BF_4)$ (**3**). (A) 10 K EPR spectrum. (B) 5 K, 7 T NIR MCD spectrum. (inset) Saturation-magnetization data (dots) and best fit (lines) collected at 13 333 cm^{-1}. C) 5 K, 7 T UV–vis MCD spectrum. Peak fits are shown for the MCD spectra as dashed lines. EPR parameters are given in the text.

1/2) that is hyperfine split by the ^{31}P ligand (I = 1/2) of the L_{PNN} moiety. The spectrum was simulated using the following parameters: g = [2.003, 2.044, 2.088] [g_{avg} = 2.045] and A(P) = [43, 40, 38] MHz [A_{avg} = 40.3 MHz] (see Supporting Information). The simulation is in excellent agreement with the experimental EPR spectrum and consistent with the assignment of **3** as a ls-Fe(I) complex. In general, a qualitative indication of the amount of spin density on a metal can be roughly estimated from the deviation of the experimental Δg value (where $\Delta g = g_{max} - g_{min}$) from the free-electron isotropic g value of 2.0023 in a frozen solution.[63] Typically, large deviations correspond to a significant spin density on the metal.[64] In this system, a Δg value of 0.085 is obtained, which suggests significant metallo-radical character being present, consistent with an unpaired electron on Fe. In Figure 9, the 5 K, 7 T NIR (Figure 9B) and UV–vis MCD spectra (Figure 9C) of **3** are shown. The saturation magnetization data collected at 13 333 cm^{-1} (Figure

DOI: 10.1021/acs.inorgchem.5b00509
Inorg. Chem. 2015, 54, 4909−4926

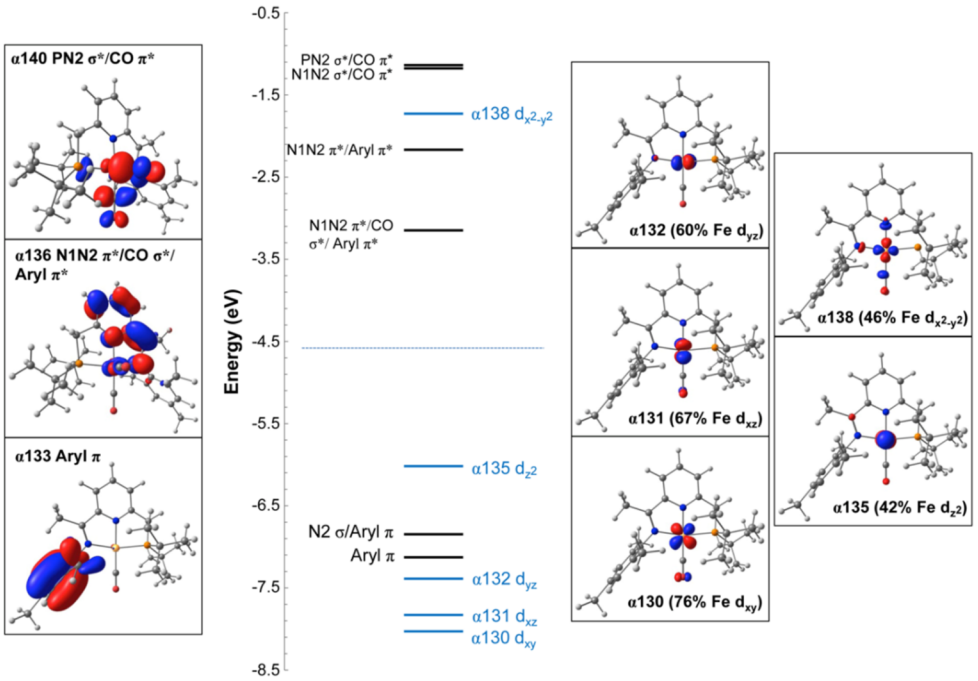

Figure 10. Calculated molecular orbital energy diagram for $[Fe(CO)_2L_{PNN}](BF_4)$ (**3**).

9B, inset) are well-described by an $S = 1/2$ ground-state model with $g = [2.003, 2.044, 2.088]$ and $(M_{xy}, M_{xz}, M_{yz}) = (0.420, 0.513, 1.022)$. The fit gives excellent agreement with the variable-temperature, variable-field (VTVH) MCD data. The transitions seen in both the NIR and UV−vis MCD spectra are fully assigned using TD-DFT (see Supporting Information). Thus, both the EPR and MCD studies support the assignment of **3** as a ls-Fe(I) ($S = 1/2$) complex.

Spin-unrestricted DFT calculations were used to further analyze the electronic structure of $[Fe(CO)_2L_{PNN}](BF_4)$ (**3**). Initial geometry optimization with PBEPBE/TZVP yielded overall structural features, bond lengths, and angles in good agreement with those observed by crystallography (see Supporting Information for details). BS calculations were performed to test the possibility of L_{PNN} acting as a redox-active ligand in this complex. Three separate calculations on the $[Fe^{I}(CO)_2(L_{PNN})]$, $[Fe^{II}(CO)_2(L_{PNN}^{-})]$ (α-spin electron from Fe → L_{PNN}), and $[Fe^{II}(CO)_2(L_{PNN}^{-})]$ (β-spin electron from Fe → L_{PNN}) electron ground-state descriptions converged to an $S_{total} = 1/2$ spin as found experimentally (see Supporting Information for details). Because of the sensitivity of these calculations toward the employed DFT functional (as seen previously for complex **2**), the B3LYP, BLYP, and HCTC functionals were utilized. Notably, all calculations, regardless of the functional, converged to the same electronic state with the unpaired electron density on Fe (MPA- and NPA-derived values of 0.86 and 0.83, respectively, from the B3LYP calculations) consistent with an $[Fe^{I}(CO)_2(L_{PNN})]$ description of complex **3** with L_{PNN} being redox-innocent. Furthermore, TD-DFT studies using this electronic structure description yield excellent agreement between the calculated and the experimentally determined d−d and CT transitions as observed in MCD and absorption spectroscopies, thus further supporting the DFT results (see Supporting Information).

The ground-state wave function of **3** is described by the FMOs with focus on the MOs in the α-spin manifold, in conjunction with their β-spin counterparts, to describe the major contributions to bonding. The MOs and the corresponding energy diagram are shown in Figure 10. In the α-spin manifold, the highest occupied molecular orbital along with the occupied α-130, α-131, and α-132, as well as the unoccupied α-138, are comprised mostly of Fe d-character, slightly mixed with L_{PNN} and CO character. The Fe d-orbitals listed in order of increasing energy are d_{xy}(α-130), d_{xz} (α-131), d_{yz} (α-132), d_{z^2} (α-135), and $d_{x^2-y^2}$ (α-138). In addition, there are FMOs that represent an occupied MO of aryl π-character (α-133), an unoccupied MO of N1N2 π*-, CO σ*-, and aryl π*-character (α-136), and an unoccupied MO of PN2 σ*- and CO π*-character (α-140).

2.4. $[Fe(F)(CO)_2L_{PNN}](BF_4)$ (4). Upon treatment of $[Fe(CO)_2L_{PNN}]$ (**2**) with 2 equiv of ferrocenium tetrafluoroborate, the iron−fluoride complex $[Fe(F)(CO)_2L_{PNN}](BF_4)$ (**4**) was obtained, and this result is likely the consequence of B−F bond cleavage of the BF_4^- counterion.[65,66] The diamagnetic complex **4** is characterized by a ^{19}F NMR shift of −428.5 ppm (d, $^2J_{FP}$ = 9.9 Hz), and the presence of the F^- ligand is also evidenced by the coupling observed in the ^{31}P NMR spectrum (δ = 106.9 ppm, d, $^2J_{PF}$ = 9.7 Hz, Table 5). Moreover, in the XPS spectra of this compound two different features for fluorine are found, one centered at ca. 685.5 eV, which is common for all BF_4^- containing complexes under study, that is, **3**, **4**, and **5**, and one feature centered at ca. 682.9 eV, which is unique for this complex and corresponds to the iron-bound F ligand. The IR stretches of 2015 and 2052 cm^{-1} in an ∼1:1 ratio confirm the presence of two CO ligands with an ∼90° angle between each other. Moreover, in the ^{13}C NMR spectrum two separate sets of signals centered at 208.1 ppm (dd, $^2J_{CP}$ = 7.0 Hz, $^2J_{CF}$ = 22.4 Hz) and 209.9 ppm (dd, $^2J_{CP}$ = 18.5 Hz, $^2J_{CF}$ = 35.9 Hz) are evidence for the presence of two distinguishable CO ligands, which must be consequently coordinated in a *cis* arrangement, and this interpretation is in agreement with the ^1H and ^{13}C NMR data as well as the crystal structure of $[Fe(F)(CO)_2L_{PNN}](BF_4)$ (**4**) (Figure 11a).

DOI: 10.1021/acs.inorgchem.5b00509
Inorg. Chem. 2015, 54, 4909−4926

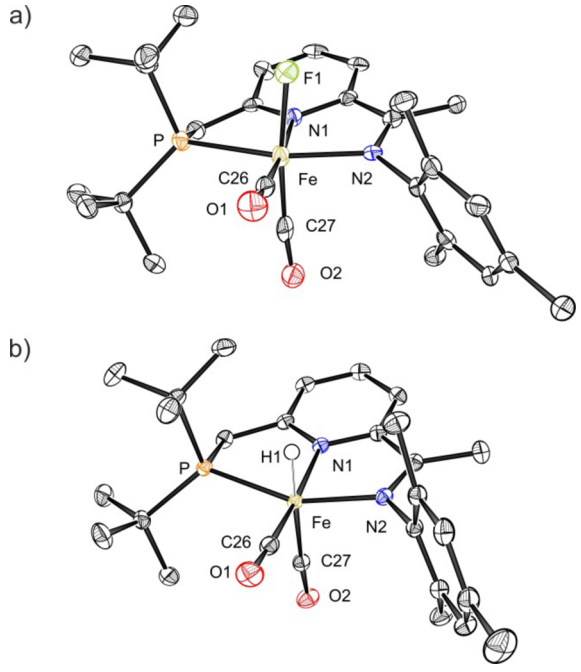

Figure 11. Molecular structures of (a) $[Fe(F)(CO)_2L_{PNN}](BF_4)$ (**4**) and (b) $[Fe(H)(CO)_2L_{PNN}](BF_4)$ (**5**) with 50% probability thermal ellipsoids. The hydrogen atoms and the BF_4^- counter are omitted for clarity. Selected bond lengths are given in Table 1

While the Mössbauer parameters of **4** at 80 K (δ = 0.04 mm s^{-1}, ΔE_Q = 0.55 mm s^{-1}, Table 2) are in the range for a ls-Fe(II) complex,[48] they are also similar to the parameters determined for **2**, assigned as an Fe(0) complex. A ls-Fe(II) assignment of **4**, however, is consistent with the blue shift of the IR stretches relative to **2** and **3**, which indicates decreased electron density at the Fe center (see Table 4). Moreover, the XPS measurements yield an Fe $2p_{3/2}$ electron binding energy of 709.9 eV (entry 10 in Table 3), which is 1.1 eV higher than for the Fe(I) complex $[Fe(CO)_2L_{PNN}](BF_4)$ (**3**). This observation is consistent with the assignment of $[Fe(F)(CO)_2L_{PNN}](BF_4)$ (**4**) as an Fe(II) complex with a neutral PNN ligand. Note that the ^{13}C NMR chemical shift of the imine carbon atom C7 is the highest among all but the carbonyl carbon-atom shifts. This observation is in line with the interpretation of a neutral PNN ligand. The C═N, C_{imine}–C_{ipso}, and C_{ipso}–N_{py} bond lengths in complex **4** are intermediate between the values for the hs-Fe(II) complex $[FeBr_2L_{PNN}]$ (**1**) and the ls-Fe(I) complex $[Fe(CO)_2L_{PNN}](BF_4)$ (**3**) (see Table 1). These parameters cannot be interpreted within the framework of the "metrical oxidation state" concept in a straightforward fashion. While a minor shift of electron density from the metal to the ligand might be indicated, the fact that the change does not come in an integer fashion is strongly indicative of a backbonding effect. In addition, DFT calculations using B3LYP, BLYP, PBEPBE, and HCTC functionals on **5** are indicative of a ls-Fe(II) complex (S = 0), consistent with the experimental data (see Supporting Information for details).

2.5. $[Fe(H)(CO)_2L_{PNN}](BF_4)$ (5). The reaction of $[Fe(CO)_2L_{PNN}]$ (**2**) with an excess of $HBF_4{\cdot}Et_2O$ in THF at room temperature gives rise to the formation of $[Fe(H)(CO)_2L_{PNN}](BF_4)$ (**5**). This diamagnetic, formal Fe(II) complex is characterized by a hydride resonance in the ^1H NMR spectrum centered at −4.59 ppm (d, 1H, $^3J_{HP}$ = 58.2 Hz, Fe–*H*). The IR stretches of 1973 and 2022 cm^{-1} in a 1:1 ratio (see Table 4) indicate a cis arrangement of two CO ligands. The presence of two chemically inequivalent CO ligands is clearly indicated by the two different sets of resonances in the ^{13}C NMR spectrum at 205.0 ppm (d, $^2J_{CP}$ = 7.8 Hz, CO) and 212.0 ppm (d, $^2J_{CP}$ = 19.3 Hz, CO), and in the ^1H NMR spectrum the two sides of the molecule (as defined by the pyridine-ring plane) can be distinguished based on the assignment of the ^{t}Bu groups, the methylene protons, and the shifts of the mesitylene unit (see Experimental Section). The crystal structure (Figure 11b) is further in agreement with the hydride being in apical position. The Mössbauer data at 80 K (δ = −0.04 mm s^{-1}, ΔE_Q = 1.48 mm s^{-1}, Table 2) are in agreement with a ls-Fe(II) interpretation of this complex.[48] In the XPS experiments, however, $[Fe(H)(CO)_2L_{PNN}](BF_4)$ (**5**) exhibits a 0.7 eV lower Fe $2p_{3/2}$ binding energy than $[Fe(F)(CO)_2L_{PNN}](BF_4)$ (**4**), the latter of which is clearly an Fe(II) compound. The difference in the iron electron-binding energies of **4** and **5** is most likely the result of the hydride ligand carrying less electron density compared to the fluoride ligand in complex **4**. This also makes sense chemically as the hydride complex **5** readily reacts with various bases such as KO^{t}Bu or KHMDS to regenerate the parent compound $[Fe(CO)_2L_{PNN}]$ (**2**); thus, the hydride ligand in **5** has quite a protic character, and this observation is reflected in the XPS data as well. Moreover, the CO stretches in the IR spectrum of the hydride complex **5** are in agreement with this interpretation (see Table 4) as they are by ca. 35 cm^{-1} lower than for the corresponding fluoride complex **4**, thus indicating increased electron density at the metal center. As was observed for $[Fe(F)(CO)_2L_{PNN}](BF_4)$ (**4**), the ^{13}C NMR chemical shift of the imine carbon atom C7 of **5** as well as the crystal structure data are essentially in agreement with the presence of a neutral PNN ligand. Consequently, the difference in electron density on the Fe centers in **4** and **5** reflects fluoride versus hydride ligation and is not a consequence of redox non-innocence of the PNN ligand. Lastly, spin-restricted DFT calculations of **5** using B3LYP are indicative of a ls-Fe(II) complex (S = 0; see Supporting Information for details).

3. DISCUSSION

The determination of ligand redox non-innocence has become an important aspect of coordination chemistry due to the importance of redox non-innocent complexes in catalysis. Toward this goal, the use of ligand structural parameters to identify systems that feature electron transfer to ligands (i.e., redox non-innocence), as demonstrated by Wieghardt and co-workers, represents a simple, structure-based method for this determination but is not unequivocal. Alternatively, studies combining spectroscopic methods aimed at the direct determination of the electronic structure of the complex as well as the metal electron density combined with DFT studies can permit the determination of ligand redox non-innocence, though such approaches are more time-consuming and require specialized instrumentation and expertise. In the present study, both approaches were utilized to evaluate electronic structure and ligand redox non-innocence in a series of PNN-ligated iron complexes ranging in formal oxidation state from Fe(0) to Fe(II), including possible backbonding versus electron-transfer effects. While ligand reduction as a consequence of electron transfer would result in changes of the ligand geometry, the ligand would be negatively charged. By contrast, backbonding from the metal center to a ligand can serve as a compensation mechanism to avoid the accumulation of negative charge

DOI: 10.1021/acs.inorgchem.5b00509
Inorg. Chem. 2015, 54, 4909−4926

density on the metal center when combined with donation from a ligand to the metal. While in a completely balanced situation the ligand would be neutral, its structure can be influenced since donation and back-donation will involve different ligand orbitals.

For the iron−dibromide complex [$FeBr_2L_{PNN}$] (**1**), ligand structural parameters indicate the presence of a neutral α-iminopyridine ligand (see Figure 12).[17−19] Thus, **1** would be

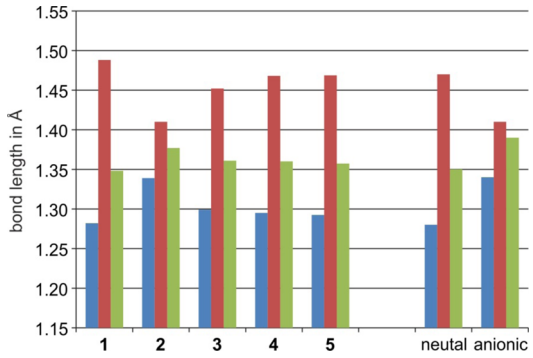

Figure 12. Comparison of the C═N (blue), C_{imine}−C_{ipso} (red), and C_{ipso}−N_{py} (green) bond lengths for complexes **1**−**5** as determined via X-ray crystallography together with the expected values for the neutral and the monoanionic form of α-iminopyridine ligands when bound to a metal center according to Wieghardt and co-workers.[17−19]

assigned as an Fe(II) complex, and Mössbauer, MCD, XPS, and DFT studies as well as magnetic measurements further support the assignment of **1** as an hs Fe(II) complex with a redox-innocent PNN ligand. Consistency between the structural and spectroscopic/theoretical methods for the determination of ligand redox non-innocence are also found for the formal Fe(II) complexes [$Fe(F)(CO)_2L_{PNN}$](BF_4) (**4**) and [$Fe(H)(CO)_2L_{PNN}$](BF_4) (**5**). For these complexes, the ligand structures are near to those expected for neutral α-iminopyridine ligands (Figure 12), consistent with the assignment of **4** and **5** as ls-Fe(II) complexes. Electronic absorption spectroscopic studies (the latter assigned using TD-DFT) combined with DFT studies also support the assignments of **4** and **5** as ls-Fe(II) complexes carrying redox-innocent PNN ligands, while according to IR spectroscopy and XPS, the electron density on the iron center is considerably lower for **4** than for **5** due to the highly electron-accepting fluoride ligand. Still, for the hs- and ls-Fe(II) L_{PNN} complexes, clearly the ligand-structural parameter approach to the determination of ligand redox non-innocence provides a simple method consistent with more extensive electronic-structure methods.

In contrast to the Fe(II)-PNN complexes, the ligand structural features of [$Fe(CO)_2L_{PNN}$](BF_4) (**3**) are between those of the neutral and the anionic descriptions (see Figure 12), and consequently one might assign a charge state of −0.5 to the PNN ligand based solely on the ligand structural parameters.[3] This interpretation, however, is in contrast to the expectations for electron transfer being responsible for the structural changes as near integer charges would be observed. Thus, for **3** the simple ligand structural parameter method for the determination of ligand redox non-innocence is insufficient. While detailed spectroscopic and theoretical studies support an Fe(I) species (with a neutral PNN ligand), the origin of the ligand structural changes remain undefined in the absence of electron transfer (i.e., ligand redox non-innocence). However, significant Fe(I)-PNN back-donation in **3** might also result in the observed ligand structural variations. Changes in the populations of the occupied and unoccupied fragment orbitals of the L_{PNN} ligand, when the metal−ligand electronic interactions are "turned on", can be utilized to quantitate donation and back-donation in this series of CO-ligated complexes (Table 6).[67]

Table 6. Donation and Back Donation between the L_{PNN} and the Metal Fragments in [$Fe(X)(CO)_2L_{PNN}$]$^{0/+}$ (X = empty, F, H) Complexes Calculated from Changes in Populations of Occupied and Unoccupied Fragment Orbitals of the Ligand

complex	total donation (α + β)	total backdonation (α + β)
[$Fe(CO)_2L_{PNN}$] (**2**)	1.28 e^-	1.14 e^-
[$Fe(CO)_2L_{PNN}$]$^+$ (**3**)	1.34 e^-	0.43 e^-
[$Fe(F)(CO)_2L_{PNN}$]$^+$ (**4**)	1.51 e^-	0.27 e^-
[$Fe(H)(CO)_2L_{PNN}$]$^+$ (**5**)	1.46 e^-	0.34 e^-

From this analysis, back-donation increases on going from the ls-Fe(II) complexes **4** and **5** to the Fe(I) complex **3**. This trend is consistent with increased back-donation contributing to ligand structural changes as the ligand acceptor orbital is a π*-orbital of L_{PNN} that is antibonding with respect to the N_1−C_6 and N_2−C_7 bond and bonding with respect to C_6−C_7 bond (vide infra).

Lastly, for [$Fe(CO)_2L_{PNN}$] (**2**) the ligand structural features are very close to those of an anionic α-iminopyridine ligand (Figure 12), and thus, **2** would be assigned as an Fe(I) complex based on the ligand structural parameter method. The accumulation of electron density on the ligand is further indicated by NMR spectroscopy: While for the free PNN ligand as well as for the ls-Fe(II) complexes **4** and **5** the imine carbon atom C7 exhibits the highest ^{13}C chemical shift among the quaternary carbon atoms C2, C6, and C7, in complex **2**, the ^{13}C NMR resonance of C7 is shifted particularly to higher field (Table 5), which might be expected according to Figure 1b if electron density is shifted to the ligand. Further, the ^{15}N chemical shift of N2 is nearly identical for complexes **4** and **5**, while it is shifted upfield by ca. 15 ppm, indicating that N2 might have some amide character[68] as expected according to Figure 1b. Notably, the ^{15}N chemical shifts of N1 are within the same range for **2**, **4**, and **5**, and this observation indicates that, if present, non-innocence does not influence the character of the pyridine nitrogen atom.[69] While both the crystallographic and the NMR data support an Fe(I) formulation of [$Fe(CO)_2L_{PNN}$] (**2**), it is important to note that both techniques provide only indirect evidence for the metal oxidation state. XPS offers the possibility to estimate the oxidation state of **2** in a more direct manner. Going from [$Fe(CO)_2L_{PNN}$] (**2**) via [$Fe(CO)_2L_{PNN}$](BF_4) (**3**) to [$Fe(F)(CO)_2L_{PNN}$](BF_4) (**4**) (entries 5, 9, and 10 in Table 3), that is, from a formal Fe(0) via a formal Fe(I) to a formal Fe(II) compound, steps of 0.7 and 1.1 eV separate the respective species, and [$Fe(CO)_2L_{PNN}$] (**2**) corresponds to the most reduced compound; this fact is also reflected in the IR stretches of the three compounds (Table 4). Since it has been demonstrated that [$Fe(CO)_2L_{PNN}$](BF_4) (**3**) and [$Fe(F)(CO)_2L_{PNN}$](BF_4) (**4**) are ls-Fe(I) and ls-Fe(II) complexes, respectively, and considering that ∼1 eV steps separate integer oxidation states for similar complexes,[50] [$Fe(CO)_2L_{PNN}$] (**2**) would be most consistent with having an Fe(0) oxidation state, as supported by XPS and IR measurements. This assignment is

DOI: 10.1021/acs.inorgchem.5b00509
Inorg. Chem. 2015, 54, 4909−4926

also consistent with TD-DFT studies combined with electronic-absorption studies, which further support Fe(0) as the oxidation state in this complex being the most consistent with the experimental data. However, BS DFT calculations clearly indicate that the Fe(I) state is close in energy to the Fe(0) state. Note that a direct correlation between the XPS Fe $2p_{3/2}$ binding energy and ν(CO) in the IR spectra was observed for the iron-dicarbonyl complexes under study (see Figure 13).

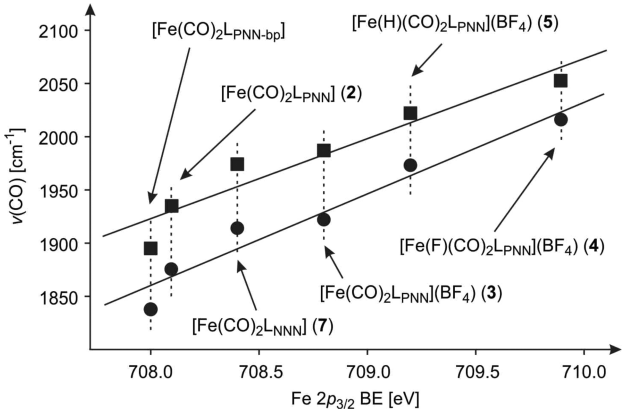

Figure 13. Correlation of ν(CO) and the XPS Fe $2p_{3/2}$ binding energies as determined in this study for complexes **2**–**5** and **7**; the values for $[Fe(CO)_2L_{PNN\text{-}bp}]$ are taken from ref 40. The squares correspond to $\nu(CO_{sym})$ (trendline with R^2 = 0.91), while the circles indicate $\nu(CO_{asym})$ (trendline with R^2 = 0.95).

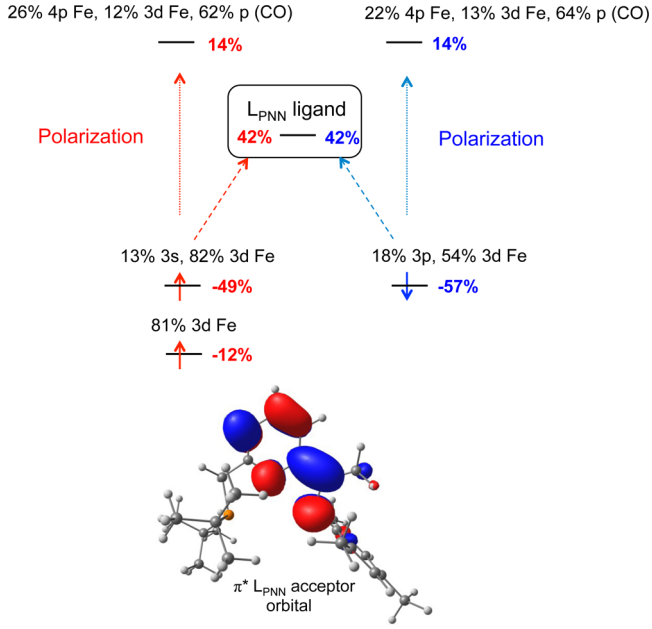

Figure 14. Fragment orbital analysis of back-donation in $[Fe(CO)_2L_{PNN}]$ (**2**) including the lowest unoccupied fragment orbital on L_{PNN} that is the acceptor orbital for back-donation. The signed changes (%) in the populations for these fragment orbitals are shown, and the negative changes indicate the loss of the electron density from a given orbital. 100% change in population corresponds to a complete transfer of an electron from an orbital.

This graph also highlights the discrepancies between the formal and the physical oxidation state description: the two formal Fe(II) complexes **4** and **5**, even though clearly identified as ls-Fe(II) complexes by spectroscopic methods, DFT calculations, and ligand structural parameters, bear a considerably different electron density on the Fe centers according to IR and XPS data.

As with complex **3**, the significant changes in the ligand structural parameters of **2** in the absence of electron transfer to the ligand can be related to significant back-donation in **2**. From the charge donation analyses (Table 6), $[Fe(CO)_2L_{PNN}]$ (**2**) exhibits a large amount of Fe → L_{PNN} back-donation (1.14 e^-) compared to the $[Fe(X)(CO)_2L_{PNN}]^{0/+}$ (X = empty, F, H) species. Fragment molecular orbital (FO) analysis of back-donation in **2** provides further insight into the origin of ligand structural changes as a result of back-donation. While electronic polarization effects are present, similar occupancy changes (~42%) are observed in both the α- and β-spin manifolds (Figure 14), and the L_{PNN} acceptor orbital for both is the lowest unoccupied fragment orbital of L_{PNN} (note that this is also the ligand acceptor orbital for back-donation in **3**). Importantly, this π^* orbital is antibonding with respect to the N_1–C_6 and the N_2–C_7 bond and bonding with respect to C_6–C_7. Hence, significant back-donation into this ligand orbital contributes to elongations of the N_1–C_6 and N_2–C_7 bonds and contraction of the C_6–C_7 bond as is observed crystallographically. Thus, significant back-donation can contribute to similar ligand bond changes as occurs with electron transfer (i.e., ligand redox non-innocence).

4. CONCLUSIONS

While Kaim's statement that "an occasional consequence from the presence of unrecognized non-innocently behaving ligands is the erroneous assignment of 'unusual' oxidation states to metals in coordination compounds"[30] is certainly valid, the use of ligand structural data alone for the determination of the metal oxidation state can also lead to erroneous interpretation of the electronic structure of transition-metal complexes. This is demonstrated in this study on a series of α-iminopyridine-based PNN-iron pincer complexes with formal oxidation states ranging from Fe(0) to Fe(II). While the crystallographic data as well as the NMR data suggest the formal Fe(0) complex $[Fe(CO)_2L_{PNN}]$ (**2**) to be an Fe(I) complex, physical measurements on the metal center combined with DFT and TD-DFT studies are more consistent with an Fe(0) center and a redox-innocent PNN ligand. This interpretation is further in line with an earlier statement that in complexes of the form $[Fe^I(CO)_2(L_{PNN}{}^{1-})]$ both the Fe(I) oxidation state and the radical ligand represent two energetically unfavorable situations assembled in one molecule.[41] We interpret the observed structural changes in terms of electron back-bonding rather than being a consequence of electron transfer. The potential importance of back-bonding contributions is particularly influenced by the finding that in $[Fe(CO)_2L_{PNN}](BF_4)$ (**3**) the PNN ligand adopts a geometry that is between the neutral and monoanionic forms combined with the significant back-donation of electron density in **2** and **3** as determined by charge donation analysis. Importantly, the PNN π^*-acceptor orbital for back-donation is such that the bond elongations observed could result from back-donation into this orbital. Overall, since a variety of factors such as the identity of the metal center and the actual ligand set determines if ligand structural changes are the consequence of back-bonding or electron transfer, it is not surprising that ligand structural parameters alone may be insufficient in many complexes for the determination of the ligand charge state (and, thus, the metal oxidation state). In

DOI: 10.1021/acs.inorgchem.5b00509
Inorg. Chem. 2015, 54, 4909–4926

these cases, a multitechnique approach combining physical methods that directly probes the electronic structure of the metal site (including XPS) combined with DFT and TD-DFT studies provides a more rigorous method for the determination of electronic structure and potential ligand redox non-innocence.

5. EXPERIMENTAL SECTION

5.1. General Considerations. All reactions were performed under a nitrogen atmosphere in a glovebox or using standard Schlenk techniques. All solvents were reagent grade or better. THF, 1,4-dioxane, diethyl ether, benzene, and pentane were refluxed over sodium and distilled under a nitrogen atmosphere. Isopropyl alcohol and triethylamine were refluxed over calcium hydride and distilled under a nitrogen atmosphere. Methylene chloride (DCM) as well as the deuterated solvents were purged with argon and stored in the glovebox over 3 Å molecular sieves. All commercially available reagents were used as received. NMR spectra were recorded using Bruker Avance III 300, Avance III 400, and Avance 500 spectrometers. Chemical shifts were referenced to the residual solvent peaks (^{1}H)[70] and to the generally accepted standards of $CDCl_3$ at 77.0 ppm, C_6D_6 at 128.0 ppm, and CD_2Cl_2 at 53.8 ppm (^{13}C), as well as to the external standards of phosphoric acid (85% solution in D_2O) at 0.0 ppm (^{31}P) and neat perfluorobenzene at −164.9 ppm (^{19}F). Chemical shifts are reported in parts per million, and coupling constants (J) are reported in hertz. NMR assignments were assisted by ^{1}H−^{1}H-COSY, ^{1}H−^{31}P-HMQC, ^{1}H−^{13}C-HSQC, ^{1}H−^{13}C-HMBC, and ^{13}C-DEPTQ NMR spectroscopy, as required. ^{15}N NMR chemical shifts were identified by ^{1}H−^{15}N-HMQC NMR measurements and are reported downfield from liquid ammonia (0.0 ppm). The effective magnetic moments in solution were measured by Evans' method at ambient temperature.[47] IR spectra were recorded on a Nicolet FT-IR spectrophotometer. UV−vis absorption measurements were performed on a Cary-5000 UV−vis−NIR spectrometer (Varian). Samples were measured in 1 × 1 cm quartz cuvettes. Electrospray ionization mass spectrometry (ESI-MS) spectra were recorded on a Micromass ZQ V4.1 by the Chemical Research Support Unit of the Weizmann Institute of Science. Elemental analyses were performed on a Thermo Finnigan Italia SpA (Flash EA 1112) C, H, N elemental analyzer by the Chemical Research Support Unit of the Weizmann Institute of Science. Note that some complexes gave unsatisfactory carbon analyses but acceptable hydrogen and nitrogen content because of a combustion problem due to the tetrafluoroborate anion,[71] and discrepancies of similar magnitude have been previously reported in such complexes.[72]

5.2. X-ray Structure Determinations. Crystal data were measured at 100 K on a Bruker Kappa Apex-II CCD diffractometer equipped with [λ(Mo Kα) = 0.710 73 Å] radiation, a graphite monochromator, and MiraCol optics. The data were processed with APEX2 collect package programs. Structures were solved by the AUTOSTRUCTURE module and refined with full-matrix least-squares refinement based on F^2 with SHELXL-97 or SHELXL-2013. Full details can be found in the CIF files and in the Supporting Information.

5.3. ^{57}Fe Mössbauer Spectroscopy. ^{57}Fe Mössbauer spectroscopic data were collected on nonenriched samples of the as-isolated complexes. All samples were prepared in an inert-atmosphere glovebox equipped with a liquid nitrogen fill port to enable sample freezing to 77 K within the glovebox. Each sample was loaded into a Delrin Mössbauer sample cup for measurements and loaded under liquid nitrogen. Low-temperature ^{57}Fe Mössbauer measurements were performed using a SEE Co. MS4 Mössbauer spectrometer integrated with a Janis SVT-400T He/N_2 cryostat for measurements at 80 K with a 0.07 T applied magnetic field. Isomer shifts were determined relative to α-Fe at 298 K. All Mössbauer spectra were fit using the program WMoss (SEE Co.).

5.4. SQUID Magnetometry. SQUID measurements were performed on a Quantum Design MPMS XL-5 SQUID magnetometer. The powdered samples were placed in gelatin capsules. The temperature dependence of the magnetic moment $M(T)$ was measured in the temperature range of $5 \leq T \leq 300$ K at external magnetic field strength of $H = 5000$ Oe, along with sample cooling and heating. Temperature steps of $\Delta T = 2$ K were chosen. Two measurements were performed at each (T, H) point to determine the standard deviation of the resulting value. Field-dependent measurements on $M(H)$ were performed at $T = 5$ K and -1000 Oe $\leq H \leq 10\,000$ Oe to check/confirm the paramagnetic behavior of the samples. The measurements were performed from 0 to 10 000 Oe with step $\Delta H = 500$ Oe and from 10 000 Oe to −1000 Oe with $\Delta H = 1000$ Oe. The molar magnetic susceptibility χ^{mol} was corrected by the sum of the Pascal coefficients calculated according to composition of the samples.[73] In the following graphs the paramagnetic contribution to the molar susceptibility is denoted as χ.

5.5. X-ray Photoelectron Spectroscopy. Powder samples were loaded to the XPS instrument via a glovebox, which was purged for several hours with N_2. XPS measurements were performed with a Kratos AXIS ULTRA system using a monochromatized Al Kα X-ray source ($h\nu$ = 1486.6 eV) at 75 W and a detection pass energy of 20 eV. A low-energy electron-flood gun was applied for charge neutralization. To define binding energies (BE) of different elements, the C 1s line at 284.8 eV was taken as a reference.[74] Curve-fitting analysis was based on linear or Shirley background subtraction and application of Gaussian−Lorentzian line shapes.

5.6. Electron Paramagnetic Resonance Spectroscopy. All samples for EPR spectroscopy were prepared in an inert atmosphere glovebox equipped with a liquid nitrogen fill port to enable sample freezing to 77 K within the glovebox. EPR samples were prepared in 4 mm OD Suprasil quartz EPR tubes from Wilmad Labglass. All samples for EPR spectroscopy were 0.95 mM in iron. X-band EPR spectra were recorded on a Bruker EMXplus spectrometer equipped with a 4119HS cavity and an Oxford ESR-900 helium flow cryostat. The instrumental parameters employed were as follows: power: 0.001 262 mW; time constant: 40.96 ms; modulation amplitude: 8 G; experimental frequency: 9.381 GHz; modulation frequency 100 kHz.

5.7. Magnetic Circular Dichroism Spectroscopy. All samples for MCD spectroscopy were prepared in an inert atmosphere glovebox equipped with a liquid nitrogen fill port to enable sample freezing to 77 K within the glovebox. MCD samples were prepared in 1:1 (v/v) THF/2-methylTHF (to form low-temperature optical glasses) in copper cells fitted with quartz disks and a 3 mm gasket. Low-temperature MCD experiments were conducted using two Jasco spectropolarimeters. Both instruments utilize a modified sample compartment incorporating focusing optics and an Oxford Instruments SM4000−7T superconducting magnet/cryostat. This setup permits measurements from 1.6 to 290 K with magnetic fields up to 7 T. A calibrated Cernox sensor directly inserted in the copper sample holder is used to measure the temperature at the sample to ±0.001 K. UV−visible (UV−vis) MCD spectra were collected using a Jasco J-715 spectropolarimeter and a shielded S-20 photomultiplier tube. Near-infrared (NIR) MCD spectra were collected with a Jasco J-730 spectropolarimeter and a liquid nitrogen cooled InSb detector. The range accessible with this NIR MCD setup is 2000−600 nm. All MCD spectra were baseline-corrected against zero-field scans. VTVH-MCD spectra were analyzed using previously reported fitting procedures.[75,76] For VTVH-MCD fitting, both negative and positive zero-field splitting models were evaluated. The reported error bars were determined via evaluation of variations of the fit parameters on the quality of the overall fit. D and $|E/D|$ values were obtained directly from the fit parameters using the relationships $E = (\delta/6)+1/3[(\delta^2/2) + \delta E_s]^{1/2}$ and $-D = E +(E_s/3) - (\delta/6)$ for $S = 2$ as previously described.[75,76]

5.8. Density Functional Theory Experimental Details. Spin-unrestricted DFT calculations were performed with the Gaussian 09 package.[77] All geometry-optimization calculations were performed with the PBEPBE exchange-correlation functional with the TZVP[78] basis set on all atoms with the inclusion of solvation effects using the polarized continuum model with THF as the solvent.[79] The geometries of all complexes were fully optimized starting from X-ray crystal structures with initial optimizations performed with CEP-4G before optimizing with the TZVP basis set. All optimized geometries have positive harmonic frequencies (confirming the calculated

DOI: 10.1021/acs.inorgchem.5b00509
Inorg. Chem. 2015, 54, 4909−4926

structures as electronic energy minima). Further calculations of molecular orbitals (MOs) and TD-DFT used the B3LYP functional with the TZVP basis set on all atoms. The analyses of the MO compositions in terms of fragment orbitals, Mayer bond orders, and the analysis of charge donation[67] were performed using the AOMix program.[80,81] Atomic charges and spin densities were calculated using Mulliken population analysis (MPA). Orbitals from the Gaussian 09 calculations were plotted with the ChemCraft program. TD-DFT was used to calculate the electronic transition energies and intensities from the ground state to the 60−80 lowest-energy excited states.

5.9. Broken Symmetry Calculations. The BS calculations of complexes **2**−**5** were completed using the B3LYP, PBEPBE, BLYP, HCTH, and M06L functionals with the TZVP basis set on all atoms (see details of calculations in terms of the functionals investigated for each complex as given in the text). In each case, two fragments were defined: L_{PNN} and Fe-$(CO)_2X_n$, where separate MO calculations were completed on both fragments. Using the AOMix-FO option, the wave functions of the two separate fragments were combined to form the wave function of the whole complex. An MO calculation was then completed for the total complex (with the SCF-converged wave function), and further electronic structure characterization was then completed in a similar manner as typical charge donation and FO analyses. Specific information regarding the BS calculations of **2** and **3** can be found in the text, while the corresponding information for **4** and **5** is as follows.

To further characterize the electronic structure of complexes **4** and **5**, BS calculations were completed to test the possibility of L_{PNN} being a redox-active ligand in these complexes. Three separate calculations were conducted for each complex to allow for the total spin (S = 0) found experimentally to stay constant, while varying the spins on the Fe and L_{PNN}. The first calculation allowed a β-spin electron to be removed from Fe (now, S = 1/2) and placed on L_{PNN}, while the second calculation allowed an α-spin electron to move from Fe (now, S = 1/2) to L_{PNN}. The final calculation allowed for a normal description of a low-spin Fe(II) (S = 0) with no unpaired electron on L_{PNN}. Notably, all calculations converged to the same energy and spin density on Fe, which is consistent with the normal description (Fe(II), S = 0) with no unpaired electrons on Fe or L_{PNN}.

5.10. Ligand Syntheses. The α-iminopyridine-based PNN ligand 2-[(di-*tert*-butylphosphino)methyl]-6-[1-(2,4,6-trimethylphenylimino)ethyl]pyridine (L_{PNN}) was synthesized in five steps (see Supporting Information, Figure S1) starting from commercially available dimethylpyridine-2,6-dicarboxylate (**A**), which was in the first two steps converted to methyl 6-(hydroxymethyl)-picolinate[82] (**B**) and 2-acetyl-6-(hydroxymethyl)pyridine[83] (**C**) according to known procedures.

2-(Hydroxymethyl)-6-[1-(mesitylimino)ethyl]pyridine (D). A mixture of 2-acetyl-6-(hydroxymethyl)pyridine (3.1 g, 20.5 mmol), freshly distilled 2,4,6-trimethylaniline (3.0 mL, 21.4 mmol), and a catalytic amount *p*-toluenesulfonic acid in 250 mL of toluene was heated for 3 h under reflux employing a Dean−Stark apparatus. The solvent was afterward evaporated, and the dark brown residue was purified by column chromatography on deactivated neutral alumina (stage II−III) with pentane/ethyl acetate (ca. 4:1). The desired product was obtained as a yellow oil. **Yield**: 75% (4.1 g).

^{1}H NMR (400 MHz, $CDCl_3$, 298 K): δ = 1.99 (s, 6H, *o*-CH_3), 2.19 (s, 3H, (C═N)−CH_3), 2.29 (s, 3H, *p*-CH_3), 3.97 (t, 1H, $^3J_{HH}$ = 4.6 Hz, O*H*), 4.82 (d, 2H, $^3J_{HH}$ = 4.2 Hz, CH_2), 6.89 (s, 2H, *m*-*H*), 7.31 (d, 1H, $^3J_{HH}$ = 7.6 Hz, *β*-*H*, P-arm side), 7.80 (vt, 1H, $^3J_{HH}$ = 7.7 Hz, *γ*-*H*), 8.28 (d, 1H, $^3J_{HH}$ = 7.8 Hz, *β*-*H*, imine side) ppm. **^{13}C{^{1}H} NMR** (101 MHz, $CDCl_3$, 298 K): δ = 16.6 (s), 17.8 (s), 20.7 (s), 63.7 (s), 119.9 (s), 121.4 (s), 125.2 (s), 128.6 (s), 132.3 (s), 137.2 (s), 146.1 (s), 155.2 (s), 157.5 (s), 166.9 (s) ppm. **MS** (ESI, methanol, m/z^+): 269.21 $[M + H]^+ = [C_{17}H_{21}N_2O]^+$, 291.22 $[M + Na]^+ = [C_{17}H_{20}N_2NaO]^+$, 559.43 $[2M+Na]^+ = [C_{34}H_{40}N_4NaO_2]^+$.

2-[(Di-*tert*-butylphosphino)methyl]-6-[1-(2,4,6-mesitylimino)ethyl]pyridine (L_{PNN}). To a solution of 2-(hydroxymethyl)-6-[1-(mesitylimino)ethyl]pyridine (4.1 g, 15.3 mmol) in 260 mL of DCM, cooled in an ice bath, were added triethylamine (8.7 mL, 62.8 mmol) and methanesulfonyl chloride (3.5 mL, 45.2 mmol). After the mixture was stirred for 30 min at 0 °C, distilled water was added, and the aqueous phase was washed several times with DCM. The combined extracts were washed with a concentrated sodium bicarbonate solution and filtered over a plug of deactivated neutral alumina (stage II−III). After it was dried over magnesium sulfate, the solvent was removed at 10 °C, and traces of solvent were removed under high vacuum at room temperature. The crude product (5.5 g) was obtained as a yellow oil and carried forward without further purification.

^{1}H NMR (500 MHz, $CDCl_3$, 298 K): δ = 1.98 (s, 6H, *o*-CH_3), 2.15 (s, 3H, (C═N)−CH_3), 2.29 (s, 3H, *p*-CH_3), 3.12 (s, 3H, O−SO_2−CH_3), 5.39 (s, 2H, CH_2), 6.89 (s, 2H, *m*-*H*), 7.55 (d, 1H, J = 7.6 Hz, *β*-*H*, P-arm side), 7.86 (vt, 1H, J = 7.8 Hz, *γ*-*H*), 8.35 (d, 1H, J = 7.9 Hz, *β*-*H*, imine side) ppm. **^{13}C{^{1}H} NMR** (126 MHz, $CDCl_3$, 298 K): δ = 16.5 (s), 17.8 (s), 20.7 (s), 38.0 (s), 71.6 (s), 121.1 (s), 123.3 (s), 125.1 (s), 128.6 (s), 132.3 (s), 137.5 (s), 146.0 (s), 152.5 (s), 156.4 (s), 167.0 (s) ppm. **MS** (ESI, methanol, m/z^+): 252.1 $[M-CH_3SO_3+H]^+ = [C_{17}H_{20}N_2]+$, 347.3 $[M + H]^+ = [C_{18}H_{23}N_2O_3S]^+$, 369.2 $[M + Na]^+ = [C_{18}H_{22}N_2NaO_3S]^+$, 715.4 $[2M+Na]^+ = [C_{36}H_{44}N_4NaO_6S_2]^+$; (ESI, methanol, m/z^-): 95.0 $[CH_3SO_3]^-$, 80.0 $[CH_4SO_2]^-$.

A solution of the crude (6-(1-(mesitylimino)ethyl)pyridin-2-yl)-methylmethanesulfonate (**E**) and di-*tert*-butylphosphine (4.0 mL, 21.6 mmol) in 60 mL of isopropyl alcohol was stirred at 50 °C for 2 d. After the addition of 10 mL of triethylamine (71.7 mmol) all volatiles were removed, and the residue was thoroughly extracted with ca. 100 mL of pentane. After filtration, the solvent was removed, and 4.3 g of a yellow oil was obtained, which contained 60−70% of the desired ligand as based on ^{1}H NMR and complexation studies (43−50% yield). For characterization purposes, ca. 100 mg of the ligand mixture was purified by column chromatography on deactivated, neutral alumina (stage II−III), employing a very thin column and pentane/diethyl ether (1:1) as the eluent. Ca. 20 mg of the pure ligand was obtained as a yellow oil. Note, however, that for the complexation reactions, the crude mixture after the extraction with pentane was used, employing appropriate amounts of the metal precursor.

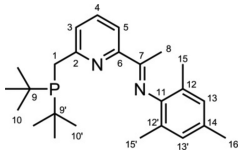

^{1}H NMR (400 MHz, $CDCl_3$, 298 K): δ = 1.20 (d, 18H, $^3J_{HP}$ = 11.0 Hz, H_{10}), 1.99 (s, 6H, H_{15}), 2.14 (s, 3H, H_8), 2.28 (s, 3H, H_{16}), 3.11 (d, 2H, $^2J_{HP}$ = 7.8 Hz, H_1), 6.87 (s, 2H, H_{13}), 7.45 (d, 1H, $^3J_{HH}$ = 7.7 Hz, H_3), 7.66 (vt, 1H, $^3J_{HH}$ = 7.75 Hz, H_4), 8.09 (d, 1H, $^3J_{HH}$ = 7.8 Hz, H_5) ppm. **^{13}C{^{1}H} NMR** (101 MHz, $CDCl_3$, 298 K): δ = 16.7 (s, C_8), 18.0 (s, C_{15}), 20.9 (s, C_{16}), 29.9 (d, $^2J_{CP}$ = 13.3 Hz, C_{10}), 31.8 (d, $^1J_{CP}$ = 24.2 Hz, C_1), 32.1 (d, $^1J_{CP}$ = 21.9 Hz, C_9), 118.1 (d, $^5J_{CP}$ = 1.7 Hz, C_5), 124.9 (d, $^3J_{CP}$ = 8.1 Hz, C_3), 125.5 (s, C_{12}), 128.6 (s, C_{13}), 132.1 (s, C_{14}), 136.6 (s, C_4), 146.5 (s, C_{11}), 155.8 (s, C_6), 161.2 (d, $^2J_{CP}$ = 14.1 Hz, C_2), 168.0 (s, C_7) ppm. **^{31}P{^{1}H} NMR** (121 MHz, $CDCl_3$, 298 K): δ = 38.5 (s) ppm. **^{15}N−^{1}H HMQC** (41 MHz, $CDCl_3$, 298 K): δ = 311.5 (s, N_1), 334.0 (s, N_2) ppm. **MS** (ESI, methanol, m/z^+): 397.37 $[M + H]^+ = [C_{25}H_{38}N_2P]^+$.

Note that 2-acetyl-6-[(di-*tert*-butylphosphino)methyl]-pyridine was identified by NMR and MS studies as one of the main impurities in the synthesis of L_{PNN}: **^{1}H NMR** (300 MHz, $CDCl_3$, 298 K): δ = 1.18 (d, 18H, $^3J_{HP}$ = 11.1 Hz, PC(CH_3)$_3$), 2.69 (s, 3H, (C═N)−CH_3), 3.10 (d, 2H, $^3J_{HP}$ = 3.1 Hz, CH_2), 7.54 (d, 1H, J = 7.7 Hz, *β*-*H*, P-arm side), 7.69 (vt, 1H, J = 7.7 Hz, *γ*-*H*), 7.80 (d, 1H, J = 7.6 Hz, *β*-*H*, imine side) ppm. **^{31}P{^{1}H} NMR** (121 MHz, $CDCl_3$, 298 K): δ = 39.2 (s) ppm. **MS** (ESI, methanol, m/z^+): 280.24 $[M + H]^+ = [C_{16}H_{27}NOP]^+$.

2,6-Bis-[1-(mesitylimino)ethyl]pyridine (L_{NNN}). 2,6-Diacetylpyridine (1.0 g, 6.2 mmol) and 2,4,6-trimethylaniline (7.0 mL, 49.9 mmol) were dissolved in 30 mL of methanol, and 10 drops of formic acid were added. The mixture was heated for 45 h to 50 °C, and precipitation of the product was completed in an ice bath. After filtration, several washings with cold methanol, and drying under high

DOI: 10.1021/acs.inorgchem.5b00509
Inorg. Chem. 2015, 54, 4909−4926

vacuum for several hours, the product was obtained as a yellow powder. **Yield**: 78% (1.95 g).

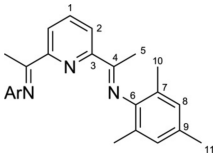

^{1}H NMR (400 MHz, $CDCl_3$, 298 K): δ = 2.04 (s, 12H, H_{10}), 2.26 (s, 6H, H_5), 2.32 (s, 6H, H_{11}), 6.92 (s, 4H, H_8), 7.92 (vt, 1H, $^3J_{HH}$ = 7.8 Hz, H_1), 8.49 (d, 2H, $^3J_{HH}$ = 7.8 Hz, H_2) ppm. **^{13}C{^{1}H} NMR** (101 MHz, $CDCl_3$, 298 K): δ = 16.4 (s, C_5), 17.9 (s, C_{10}), 20.7 (s, C_{11}), 122.1 (s, C_2), 125.2 (s, C_7), 128.6 (s, C_8), 132.2 (s, C_9), 136.8 (s, C_1), 146.3 (s, C_6), 155.2 (s, C_3), 167.4 (s, C_4) ppm. **^{15}N−^{1}H HMQC** (41 MHz, $CDCl_3$, 298 K): δ = 310.4 (s, N_1), 336.0 (s, N_2) ppm. **MS** (ESI, methanol, m/z^+): 398.3 $[M + H]^+ = [C_{27}H_{32}N_3]^+$, 420.3 $[M + Na]^+ = [C_{27}H_{31}N_3Na]^+$, 817.6 $[2M+Na]^+ = [C_{54}H_{62}N_6Na]^+$.

5.11. Complex Syntheses. *[$FeBr_2L_{PNN}$] (1).* A mixture of the crude PNN ligand (801.4 mg, contains ca. 560 mg of pure ligand, 1.412 mmol) and anhydrous $FeBr_2$ (210 mg, 0.974 mmol) in 35 mL of THF was stirred overnight. The solvent was evaporated completely, and the residue was treated with diethyl ether (in which it is nearly insoluble) under vigorous stirring for several hours. After the blue powder settled completely, the supernatant was removed, and the residue was washed several times with pentane and dried in high vacuum. Note that ^{1}H and ^{31}P NMR spectra of the supernatant indicate that only small amounts of the PNN ligand remain unreacted. Elemental analysis and Mössbauer spectroscopy unequivocally prove that no other iron-containing complexes than $[FeBr_2L_{PNN}]$ (**1**) are present in the final product. Crystals suitable for X-ray diffraction were obtained by dissolving the complex in benzene; after a while, dark blue crystals were formed. **Yield**: 96% (573.5 mg).

Anal. Calcd for $C_{25}H_{37}Br_2FeN_2P$: C, 49.05; H, 6.09; N, 4.58; Found: C, 48.53; H, 6.03; N, 4.24%. **MS** (ESI, acetonitrile, m/z^+): 531.2 $[M-Br]^+ = [C_{25}H_{37}BrFeN_2P]^+$; (ESI, acetonitrile, m/z^-): 78.9 $[Br]^-$. **Magnetic susceptibility (Evans)**: μ_{eff} = 5.4 (1,4-dioxane in $CDCl_3$, 298 K). **SQUID magnetometry**: μ_{eff} = 4.77 (at 298 K, see Supporting Information for further details). **Mössbauer**: 80 K: δ = 0.94 mm s^{-1}, ΔE_Q = 2.59 mm s^{-1}; 5 K: δ = 0.96 mm s^{-1}, ΔE_Q = 2.90 mm s^{-1}. **XPS**: Fe 709.4, N 399.5, C 284.8, P 130.5, Br 68.1 eV.

[$FeCl_2L_{PNN}$] (1′). Synthesized in analogy to $[FeBr_2L_{PNN}]$ (**1**). Crude PNN ligand (100 mg, contains ca. 70 mg of pure ligand, 0.177 mmol); $FeCl_2$ (15.4 mg, 0.122 mmol); 5 mL of THF. **Yield**: 59% (37.3 mg). **MS** (ESI, acetonitrile, m/z^+): 487.3 $[M-Cl]^+ = [C_{25}H_{37}ClFeN_2P]^+$. **XPS**: Fe 709.4, N 399.5, C 284.8, Cl 197.8, P 130.4 eV.

[$Fe(CO)_2L_{PNN}$] (2). In a 100 mL pressure flask fitted with a Teflon stopcock $[FeBr_2L_{PNN}]$ (**1**) (438 mg, 0.715 mmol) was dissolved in 30 mL of THF, and sodium amalgam (10%) (464 mg, 2.018 mmol) was added. After two freeze−pump−thaw cycles, the frozen mixture was allowed to warm to room temperature under 1 bar of CO atmosphere and was vigorously stirred overnight. After the solvent was evaporated completely, the residue was extracted with pentane (ca. 200 mL), and the solution was filtered through a syringe filter and evaporated to ca. 5 mL. After filtration through a frit, the product was obtained as a dark purple, nearly black powder. Crystals suitable for X-ray diffraction were obtained from a concentrated pentane solution at −30 °C. **Yield**: 90% (328.6 mg).

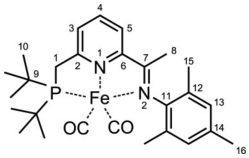

^{1}H NMR (400 MHz, C_6D_6, 298 K): δ = 0.98 (d, 18H, $^3J_{HP}$ = 12.6 Hz, H_{10}), 1.74 (s, 3H, H_8), 2.23 (s, 3H, H_{16}), 2.25 (s, 6H, H_{15}), 3.27 (d, 2H, $^2J_{HP}$ = 8.3 Hz, H_1), 6.30 (d, 1H, $^3J_{HH}$ = 6.6 Hz, H_3), 6.75 (dd, 1H, $^3J_{HH}$ = 6.6, 8.5 Hz, H_4), 6.95 (s, 2H, H_{13}), 7.04 (d, 1H, $^3J_{HH}$ = 8.5 Hz, H_5) ppm. **^{13}C{^{1}H} NMR** (101 MHz, C_6D_6, 298 K): δ = 14.7 (s, C_8), 18.8 (s, C_{15}), 21.1 (s, C_{16}), 29.3 (d, $^2J_{CP}$ = 3.8 Hz, C_{10}), 35.7 (d, $^1J_{CP}$ = 17.2 Hz, C_1), 38.0 (d, $^1J_{CP}$ = 11.3 Hz, C_9), 108.9 (d, $^3J_{CP}$ = 9.3 Hz, C_3), 121,1 (s, C_5), 124.0 (s, C_4), 129.2 (s, C_{13}), 129.8 (s, C_{12}), 133.8 (s, C_{14}), 144.7 (d, $^3J_{CP}$ = 5.1 Hz, C_6), 144.9 (s, C_7), 153.1 (s, C_{11}), 159.2 (d, $^2J_{CP}$ = 7.8 Hz, C_2), 221.1 (d, $^2J_{CP}$ = 11.3 Hz, CO) ppm. **^{31}P{^{1}H} NMR** (121 MHz, C_6D_6, 298 K): δ = 138.4 (s) ppm. **^{15}N−^{1}H HMQC** (41 MHz, C_6D_6, 298 K): δ = 258.1 (s, N_1), 259.2 (s, N_2) ppm. **IR(NaCl)**: $\tilde{\nu}$ = 1875 (ν_{CO}), 1934 cm^{-1} (ν_{CO}). **IR(pentane)**: $\tilde{V}$ = 1897 (ν_{CO}), 1952 cm^{-1} (ν_{CO}). **Anal. Calcd** for $C_{27}H_{37}FeN_2O_2P$: C, 63.78; H, 7.34; N, 5.51; Found: C, 63.16; H, 7.36; N, 5.10%. **MS** (ESI, acetonitrile, m/z^+): 480.3 $[M-CO]^+ = [C_{26}H_{37}FeN_2OP]^+$. **Magnetic susceptibility (Evans)**: μ_{eff} = 0.0 (1,4-dioxane in C_6D_6, 298 K); **Mössbauer**: 80 K: δ = 0.00 mm s^{-1}, ΔE_Q = 1.14 mm s^{-1}; 5 K: δ = 0.01 mm s^{-1}, ΔE_Q = 1.13 mm s^{-1}. **XPS**: Fe 708.1, N 398.7, C 284.8, P 130.5 eV.

[$Fe(CO)_2L_{PNN}$](BF_4) (3). In a solution of $[Fe(CO)_2L_{PNN}]$ (**2**) (107.4 mg, 0.211 mmol) in 15 mL of THF, ferrocenium tetrafluoroborate (57.5 mg, 0.211 mmol) was suspended, and the mixture was stirred for 3 h, during which the color of the solution changed from purple to green. The volume of the reaction mixture was reduced to 2 mL, and precipitation was completed by the addition of pentane. The supernatant was removed, and the dark green residue was washed several times with pentane and dried in vacuum. Crystals suitable for X-ray diffraction were grown at room temperature by slow diffusion of pentane into a THF solution. **Yield**: 96% (120.4 mg).

IR(NaCl): $\tilde{V}$ = 1922 (ν_{CO}), 1987 cm^{-1} (ν_{CO}). **Anal. Calcd** for $C_{27}H_{37}BF_4FeN_2O_2P$: C, 54.48; H, 6.27; N, 4.71; Found: C, 50.76; H, 6.37; N, 4.48%. **MS** (ESI, acetonitrile, m/z^+): 480.3 $[M-BF_4-CO]^+ = [C_{26}H_{37}FeN_2OP]^+$; (ESI, acetonitrile, m/z^-): 87.0 $[BF_4]^-$. **Magnetic susceptibility (Evans)**: μ_{eff} = 2.1 (1,4-dioxane in $CDCl_3$, 298 K). **SQUID magnetometry**: μ_{eff} = 2.14 (at 298 K, see Supporting Information for further details). **Mössbauer**: 80 K: δ = 0.12 mm s^{-1}, ΔE_Q = 0.54 mm s^{-1}; 5 K: δ = 0.12 mm s^{-1}, ΔE_Q = 0.54 mm s^{-1}. **XPS**: Fe 708.8, F 685.5, N 399.7, C 284.8, B 193.7, P 130.7 eV.

[$Fe(F)(CO)_2L_{PNN}$](BF_4) (4). In a solution of $[Fe(CO)_2L_{PNN}]$ (**2**) (165.2 mg, 0.325 mmol) in 50 mL of THF, ferrocenium tetrafluoroborate (173.9 mg, 0.637 mmol) was suspended, and the mixture was stirred in the dark for 3 h. After the precipitate settled completely, the supernatant was removed, and the dark green powder was washed once with THF and three times with pentane and dried in vacuum. Crystals suitable for X-ray diffraction were grown at room temperature by slow diffusion of pentane into a DCM solution. Note that the product is light-sensitive, particularly in solution (the identity of the decomposition product(s) remains unknown). **Yield**: 92% (179.5 mg).

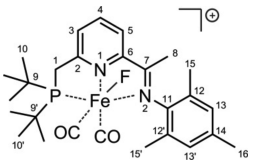

^{1}H NMR (400 MHz, CD_2Cl_2, 298 K): δ = 1.33 (d, 9H, $^3J_{HP}$ = 14.4 Hz, H_{10}'), 1.46 (d, 9H, $^3J_{HP}$ = 14.4 Hz, H_{10}), 2.11 (s, 3H, H_{15}), 2.35 (s, 3H, H_{16}), 2.38 (s, 3H, H_{15}'), 2.39 (s, 3H, H_8), 3.94 (dd, 1H, $^2J_{HP}$ = 7.2 Hz, $^2J_{HH}$ = 17.4 Hz, H_1), 4.20 (dd, 1H, $^2J_{HP}$ = 13.7 Hz, $^2J_{HH}$ = 17.4 Hz, H_1'), 7.03 (s, 1H, H_{13}), 7.08 (s, 1H, H_{13}'), 8.16 (d, 1H, $^3J_{HH}$ = 7.5 Hz, H_5), 8.20 (d, 1H, $^3J_{HH}$ = 7.7 Hz, H_3), 8.37 (vt, 1H, $^3J_{HH}$ = 7.6 Hz, H_4) ppm. **^{13}C{^{1}H} NMR** (101 MHz, CD_2Cl_2, 298 K): δ = 18.3 (s, C_{15}), 19.0 (s, C_{15}' and C_8), 20.9 (s, C_{16}), 29.7 (d, $^2J_{CP}$ = 9.9 Hz, C_{10}), 30.4 (d, $^2J_{CP}$ = 1.3 Hz, C_{10}'), 37.2 (d, $^1J_{CP}$ = 18.7 Hz, C_1), 38.2 (d, $^1J_{CP}$ = 16.1 Hz, C_9'), 40.5 (d, $^1J_{CP}$ = 11.0 Hz, C_9), 127.0 (s, C_5), 127.7 (d, $^3J_{CP}$ = 8.4 Hz, C_3), 127.8 (s, C_{12}), 130.2 (s, C_{13}), 130.8 (s, C_{12}'), 130.9 (s, C_{13}'), 138.2 (s, C_{14}), 142.1 (s, C_4), 145.3 (s, C_{11}), 156.6 (d, J_{CP} = 3.5 Hz, C_6), 164.5 (d, $^2J_{CP}$ = 2.8 Hz, C_2), 179.9 (s, C_7), 208.1 (dd, $^2J_{CP}$ = 7.0 Hz, $^2J_{CF}$ = 22.4 Hz, CO), 209.9 (dd, $^2J_{CP}$ = 18.5 Hz, $^2J_{CF}$ = 35.9 Hz, CO) ppm. **^{31}P{^{1}H} NMR** (121 MHz, CD_2Cl_2, 298 K): δ = 106.9 (d, $^2J_{PF}$ = 9.7 Hz) ppm. **^{19}F{^{1}H} NMR** (282 MHz, CD_2Cl_2, 298 K): δ

DOI: 10.1021/acs.inorgchem.5b00509
Inorg. Chem. 2015, 54, 4909−4926

= −154.5 (s, br, BF_4^-), −428.5 (d, $^2J_{FP}$ = 9.9 Hz, Fe−*F*) ppm. **^{15}N−^{1}H HMQC** (41 MHz, CD_2Cl_2, 298 K): δ = 257.6 (s, N_1), 274.1 (s, N_2) ppm. **IR(NaCl)**: $\tilde{V}$ = 2015 (ν_{CO}), 2052 cm^{-1} (ν_{CO}). **Anal. Calcd** for $C_{27}H_{37}BF_5FeN_2O_2P$: C, 52.80; H, 6.07; N, 4.56; Found: C, 51.44; H, 6.00; N, 4.27%. **MS** (ESI, acetonitrile, m/z^+): 527.3 $[M-BF_4]^+$ = $[C_{27}H_{37}FFeN_2O_2P]^+$, 471.3 $[M-BF_4-2CO]^+$ = $[C_{25}H_{37}FFeN_2P]^+$; (ESI, acetonitrile, m/z^-): 87.0 $[BF_4]^-$. **Mössbauer**: 80 K: δ = 0.04 mm s^{-1}, ΔE_Q = 0.55 mm s^{-1}; 5 K: δ = 0.04 mm s^{-1}, ΔE_Q = 0.56 mm s^{-1}. **XPS**: Fe 709.9, F 682.9 (Fe-*F*) and 685.5 (BF_4^-), N 399.8, C 284.8, B 193.9, P 130.8 eV.

[Fe(H)(CO)$_2$L$_{PNN}$](BF$_4$) (5). To a solution of $[Fe(CO)_2L_{PNN}]$ (**2**) (196 mg, 0.386 mmol, 1 equiv) in 30 mL of THF, an excess of $HBF_4{\cdot}Et_2O$ (ca. 50 drops, ca. 10 equiv) was added, and the mixture was stirred at room temperature for 2 h, during which the color changed from purple to green. The solvent volume was reduced to a third, and the raw product was precipitated by the addition of pentane. The supernatant was removed, and the residue was treated for 2 h with diethyl ether under vigorous stirring. After the green powder settled completely, the supernatant was removed, and the residue was washed several times with pentane and dried in high vacuum. The residue was taken up in DCM, filtered, and precipitated by dropping the solution into diethyl ether while stirring. This procedure aided in removing presumable paramagnetic impurities of unknown identity that caused broadened lines in the NMR spectra. The precipitate was washed once with diethyl ether and dried in vacuum. Crystals suitable for X-ray diffraction were grown by slow diffusion of pentane into a DCM solution. **Yield**: 89% (204.7 mg).

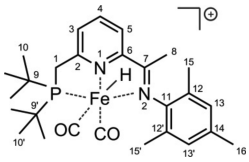

^{1}H NMR (400 MHz, $CDCl_3$, 298 K): δ = −4.59 (d, 1H, $^2J_{HP}$ = 58.2 Hz, Fe−*H*), 1.28 (d, 9H, $^3J_{HP}$ = 14.2 Hz, H_{10}'), 1.40 (d, 9H, $^3J_{HP}$ = 14.5 Hz, H_{10}), 2.23 (s, 3H, H_{15}), 2.25 (s, 3H, H_{15}'), 2.28 (s, 3H, H_8), 2.33 (s, 3H, H_{16}), 3.73 (dd, 1H, $^2J_{HP}$ = 6.4 Hz, $^2J_{HH}$ = 18.0 Hz, H_1), 4.24 (dd, 1H, $^2J_{HP}$ = 13.4 Hz, $^2J_{HH}$ = 18.1 Hz, H_1'), 7.00 (s, 1H, H_{13}'), 7.02 (s, 1H, H_{13}), 8.13 (m, 1H, H_5), 8.16 (m, 1H, H_3), 8.16 (m, 1H, H_4) ppm. **^{13}C{^{1}H} NMR** (101 MHz, $CDCl_3$, 298 K): δ = 17.4 (s, C_8), 18.0 (s, C_{15}), 18.3 (s, C_{15}'), 20.8 (s, C_{16}), 27.3 (s, C_{10}'), 30.1 (d, $^2J_{CP}$ = 2.3 Hz, C_{10}), 37.0 (d, $^1J_{CP}$ = 19.0 Hz, C_1), 37.5 (d, $^1J_{CP}$ = 16.2 Hz, C_9), 38.4 (d, $^1J_{CP}$ = 22.0 Hz, C_9'), 125.8 (s, C_5), 126.5 (d, $^3J_{CP}$ = 8.6 Hz, C_3), 126.9 (s, C_{12}), 127.3 (s, C_{12}'), 129.9 (s, C_{13}), 130.1 (s, C_{13}'), 137.0 (s, C_{14}), 139.5 (s, C_4), 145.9 (s, C_{11}), 153.9 (d, J_{CP} = 4.3 Hz, C_6), 162.4 (d, $^2J_{CP}$ = 4.0 Hz, C_2), 173.3 (s, C_7), 205.0 (d, $^2J_{CP}$ = 7.8 Hz, *C*O), 212.0 (d, $^2J_{CP}$ = 19.3 Hz, *C*O) ppm. **^{31}P{^{1}H} NMR** (121 MHz, $CDCl_3$, 298 K): δ = 120.3 (s) ppm. **^{19}F{^{1}H} NMR** (282 MHz, $CDCl_3$, 298 K): δ = −154.5 (s, br, BF_4^-) ppm. **^{15}N−^{1}H HMQC** (41 MHz, $CDCl_3$, 298 K): δ = 258.6 (s, N_1), 274.8 (s, N_2) ppm. **IR(NaCl)**: $\tilde{V}$ = 1929 (ν_{Fe-H}), 1973 (ν_{CO}), 2022 cm^{-1} (ν_{CO}). **Anal. Calcd** for $C_{27}H_{38}BF_4FeN_2O_2P$: C, 54.39; H, 6.42; N, 4.70; Found: C, 51.44; H, 6.20; N, 4.21%. **MS** (ESI, acetonitrile, m/z^+): 509.3 $[M-BF_4]^+$ = $[C_{27}H_{38}FeN_2O_2P]^+$, 481.3 $[M-BF_4-CO]^+$ = $[C_{26}H_{38}FeN_2OP]^+$; (ESI, acetonitrile, m/z^-): 87.0 $[BF_4]^-$. **Mössbauer**: 80 K: δ = −0.04 mm s^{-1}, ΔE_Q = 1.48 mm s^{-1}. **XPS**: Fe 709.2, F 685.5, N 399.9, C 284.8, B 193.6, P 130.9 eV.

[FeBr$_2$L$_{NNN}$] (6). A mixture of 2,6-bis-[1-(mesitylimino)ethyl]-pyridine (455 mg, 1.144 mmol) and anhydrous $FeBr_2$ (233 mg, 1.080 mmol) in 50 mL of THF was stirred overnight. The volume was reduced to one-third, the product was precipitated by the addition of 50 mL of diethyl ether, and the mixture was stirred for several hours. After the blue powder settled completely, the supernatant was removed, and the residue was washed several times with diethyl ether and dried under vacuum. **Yield**: 96% (635.8 mg). **MS** (ESI, acetonitrile, m/z^+): 532.2 $[M-Br]^+$ = $[C_{27}H_{31}BrFeN_3]^+$; (ESI, acetonitrile, m/z^-): 78.9 $[Br]^-$. **XPS**: Fe 709.7, N 399.5, C 284.8, Br 68.2 eV.

[Fe(CO)$_2$L$_{NNN}$] (7). In a 100 mL pressure flask fitted with a Teflon stopcock, sodium amalgam (10%, 390 mg, 1.696 mmol) was added to 0.8 mL of mercury in 5 mL of THF, and the mixture was stirred until the amalgam was dissolved in the mercury. To this mixture a suspension of $[FeBr_2L_{NNN}]$ (**6**) (506 mg, 0.825 mmol) in 25 mL of THF was added. After two freeze−pump−thaw cycles, the frozen mixture was allowed to warm to room temperature under 1 bar of CO atmosphere and was vigorously stirred overnight. After the solvent was evaporated completely, the residue was extracted with ether (ca. 500 mL), and the solution was filtrated through a syringe filter and evaporated to ca. 5 mL. After filtration through a frit, the product was obtained as a dark green powder. Crystals suitable for X-ray diffraction were obtained by slow diffusion of pentane into a DCM solution. **Yield**: 71% (296.3 mg).

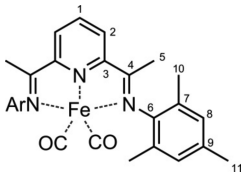

^{1}H NMR (400 MHz, C_6D_6, 298 K): δ = 2.01 (s, 12H, H_{10}), 2.01 (s, 6H, H_5), 2.08 (s, 6H, H_{11}), 6.78 (m, 4H, H_8), 7.20 (vt, 1H, $^3J_{HH}$ = 7.7 Hz, H_1), 7.77 (d, 2H, $^3J_{HH}$ = 7.7 Hz, H_2) ppm. **^{13}C{^{1}H} NMR** (101 MHz, C_6D_6, 298 K): δ = 15.0 (s, C_5), 18.3 (s, C_{10}), 20.9 (s, C_{11}), 116.2 (s, C_1), 120.6 (s, C_2), 129.1 (s, C_7), 129.3 (s, C_8), 134.8 (s, C_9), 145.0 (s, C_3), 150.7 (s, C_6), 154.9 (s, C_4), 215.1 (s, CO) ppm. **^{15}N−^{1}H HMQC** (41 MHz, C_6D_6, 298 K): δ = 248.7 (s, N_1), 255.2 (s, N_2). **IR(NaCl)**: $\tilde{V}$ = 1878 (ν_{CO}), 1949 cm^{-1} (ν_{CO}). **Mössbauer**: 80 K: δ = 0.00 mm s^{-1}, ΔE_Q = 1.44 mm s^{-1}. **XPS**: Fe 708.4, N 398.9, C 284.8 eV.

■ ASSOCIATED CONTENT

Ⓢ Supporting Information

Schematic illustration of synthesis including reaction conditions, Mössbauer spectra, EPR simulations, electronic absorption spectra, SQUID data, XPS spectra, X-ray structural data; calculated MO diagrams, broken symmetry calculations, DFT-optimized geometry coordinates, TD-DFT. This material is available free of charge via the Internet at http://pubs.acs.org.

■ AUTHOR INFORMATION

Corresponding Authors

*E-mail: neidig@chem.rochester.edu. (M.L.N.)
*E-mail: david.milstein@weizmann.ac.il. (D.M.)

Author Contributions

⊥These authors contributed equally.

Notes

The authors declare no competing financial interest.

■ ACKNOWLEDGMENTS

We would like to thank Prof. B. Rybtchinsky and Prof. M. v. d. Boom who allowed us to use their UV−vis spectrometry and CV equipment, respectively. This research was supported by the European Research Council under the FP7 framework (ERC No. 246837), the MINERVA Foundation, and the Univ. of Rochester (M.L.N.). B.B. received the Feodor-Lynen postdoctoral fellowship from the Alexander von Humboldt Foundation, and D.M. holds the Israel Matz Professorial Chair of Organic Chemistry. The authors also acknowledge the Center for Integrated Research Computing at the Univ. of Rochester for providing the necessary computing systems and support to enable the computational research presented in this study.

DOI: 10.1021/acs.inorgchem.5b00509
Inorg. Chem. 2015, 54, 4909−4926

REFERENCES

(1) Klein, J. E. M. N.; Miehlich, B.; Holzwarth, M. S.; Bauer, M.; Milek, M.; Khusniyarov, M. M.; Knizia, G.; Werner, H.-J.; Plietker, B. *Angew. Chem., Int. Ed.* **2014**, *53*, 1790−1794.
(2) Evans, W. J.; Fang, M.; Bates, J. E.; Furche, F.; Ziller, J. W.; Kiesz, M. D.; Zink, J. I. *Nat. Chem.* **2010**, *2*, 644−647.
(3) Brown, S. N. *Inorg. Chem.* **2012**, *51*, 1251−1260.
(4) Zanello, P.; Corsini, M. *Coord. Chem. Rev.* **2006**, *250*, 2000−2022.
(5) Pierpont, C. G. *Coord. Chem. Rev.* **2001**, *216−217*, 99−125.
(6) Papavassiliou, G. C.; Anyfantis, G. C.; Mousdis, G. A. *Crystals* **2012**, *2*, 762−811.
(7) Broere, D. L. J.; de Bruin, B.; Reek, J. N. H.; Lutz, M.; Dechert, S.; van der Vlugt, J. I. *J. Am. Chem. Soc.* **2014**, *136*, 11574−11577.
(8) Smith, A. L.; Hardcastle, K. I.; Soper, J. D. *J. Am. Chem. Soc.* **2010**, *132*, 14358−14360.
(9) Chaudhuri, P.; Verani, C. N.; Bill, E.; Bothe, E.; Weyhermüller, T.; Wieghardt, K. *J. Am. Chem. Soc.* **2001**, *123*, 2213−2223.
(10) Bowman, A. C.; England, J.; Sproules, S.; Weyhermüller, T.; Wieghardt, K. *Inorg. Chem.* **2013**, *52*, 2242−2256.
(11) Bowman, A. C.; Sproules, S.; Wieghardt, K. *Inorg. Chem.* **2012**, *51*, 3707−3717.
(12) England, J.; Scarborough, C. C.; Weyhermüller, T.; Sproules, S.; Wieghardt, K. *Eur. J. Inorg. Chem.* **2012**, 4605−4621.
(13) Irwin, M.; Doyle, L. R.; Krämer, T.; Herchel, R.; McGrady, J. E.; Goicoechea, J. M. *Inorg. Chem.* **2012**, *51*, 12301−12312.
(14) Scarborough, C. C.; Wieghardt, K. *Inorg. Chem.* **2011**, *50*, 9773−9793.
(15) Scarborough, C. C.; Sproules, S.; Weyhermüller, T.; DeBeer, S.; Wieghardt, K. *Inorg. Chem.* **2011**, *50*, 12446−12462.
(16) Irwin, M.; Jenkins, R. K.; Denning, M. S.; Krämer, T.; Grandjean, F.; Long, G. J.; Herchel, R.; McGrady, J. E.; Goicoechea, J. M. *Inorg. Chem.* **2010**, *49*, 6160−6171.
(17) Lu, C. C.; Weyhermüller, T.; Bill, E.; Wieghardt, K. *Inorg. Chem.* **2009**, *48*, 6055−6064.
(18) Lu, C. C.; Bill, E.; Weyhermüller, T.; Bothe, E.; Wieghardt, K. *J. Am. Chem. Soc.* **2008**, *130*, 3181−3197.
(19) Lu, Connie C.; DeBeer George, S.; Weyhermüller, T.; Bill, E.; Bothe, E.; Wieghardt, K. *Angew. Chem., Int. Ed.* **2008**, *47*, 6384−6387.
(20) Darmon, J. M.; Stieber, S. C. E.; Sylvester, K. T.; Fernández, I.; Lobkovsky, E.; Semproni, S. P.; Bill, E.; Wieghardt, K.; DeBeer, S.; Chirik, P. J. *J. Am. Chem. Soc.* **2012**, *134*, 17125−17137.
(21) Stieber, S. C. E.; Milsmann, C.; Hoyt, J. M.; Turner, Z. R.; Finkelstein, K. D.; Wieghardt, K.; DeBeer, S.; Chirik, P. J. *Inorg. Chem.* **2012**, *51*, 3770−3785.
(22) Bowman, A. C.; Milsmann, C.; Atienza, C. C. H.; Lobkovsky, E.; Wieghardt, K.; Chirik, P. J. *J. Am. Chem. Soc.* **2010**, *132*, 1676−1684.
(23) Bart, S. C.; Lobkovsky, E.; Bill, E.; Wieghardt, K.; Chirik, P. J. *Inorg. Chem.* **2007**, *46*, 7055−7063.
(24) Bart, S. C.; Chłopek, K.; Bill, E.; Bouwkamp, M. W.; Lobkovsky, E.; Neese, F.; Wieghardt, K.; Chirik, P. J. *J. Am. Chem. Soc.* **2006**, *128*, 13901−13912.
(25) Knijnenburg, Q.; Gambarotta, S.; Budzelaar, P. H. M. *Dalton Trans.* **2006**, 5442−5448.
(26) de Bruin, B.; Bill, E.; Bothe, E.; Weyhermüller, T.; Wieghardt, K. *Inorg. Chem.* **2000**, *39*, 2936−2947.
(27) Chang, M.-C.; Dann, T.; Day, D. P.; Lutz, M.; Wildgoose, G. G.; Otten, E. *Angew. Chem., Int. Ed.* **2014**, *53*, 4118−4122.
(28) Zhou, W.; Patrick, B. O.; Smith, K. M. *Chem. Commun.* **2014**, *50*, 9958−9960.
(29) Lyaskovskyy, V.; de Bruin, B. *ACS Catal.* **2012**, *2*, 270−279.
(30) Kaim, W. *Inorg. Chem.* **2011**, *50*, 9752−9765.
(31) Adhikari, D.; Mossin, S.; Basuli, F.; Huffman, J. C.; Szilagyi, R. K.; Meyer, K.; Mindiola, D. J. *J. Am. Chem. Soc.* **2008**, *130*, 3676−3682.
(32) Butin, K. P.; Beloglazkina, E. K.; Zyk, N. V. *Russ. Chem. Rev.* **2005**, *74*, 531−553.
(33) Evangelio, E.; Ruiz-Molina, D. *Eur. J. Inorg. Chem.* **2005**, 2957−2971.
(34) Luca, O. R.; Crabtree, R. H. *Chem. Soc. Rev.* **2013**, *42*, 1440−1459.
(35) Praneeth, V. K. K.; Ringenberg, M. R.; Ward, T. R. *Angew. Chem., Int. Ed.* **2012**, *51*, 10228−10234.
(36) Chirik, P. J.; Wieghardt, K. *Science* **2010**, *327*, 794−795.
(37) http://goldbook.iupac.org/O04365.html.
(38) Leigh, V.; Carleton, D. J.; Olguin, J.; Mueller-Bunz, H.; Wright, L. J.; Albrecht, M. *Inorg. Chem.* **2014**, *53*, 8054−8060.
(39) Gore-Randall, E.; Irwin, M.; Denning, M. S.; Goicoechea, J. M. *Inorg. Chem.* **2009**, *48*, 8304−8316.
(40) Zell, T.; Milko, P.; Fillman, K. L.; Diskin-Posner, Y.; Bendikov, T.; Iron, M. A.; Leitus, G.; Ben-David, Y.; Neidig, M. L.; Milstein, D. *Chem.—Eur. J.* **2014**, *20*, 4403−4413.
(41) Milko, P.; Iron, M. A. *J. Chem. Theory Comput.* **2013**, *10*, 220−235.
(42) Tondreau, A. M.; Milsmann, C.; Lobkovsky, E.; Chirik, P. J. *Inorg. Chem.* **2011**, *50*, 9888−9895.
(43) Bart, S. C.; Lobkovsky, E.; Chirik, P. J. *J. Am. Chem. Soc.* **2004**, *126*, 13794−13807.
(44) Note that a similar ligand bearing an O−P instead of a CH_2−P arm was synthesized before, and the corresponding $FeBr_2$ and $Fe(CO)_2$ complexes were also described. The focus of the studies, however, was on catalytic hydrosilylation reactions rather than on the electronic nature of the complexes: Peng, D.; Zhang, Y.; Du, X.; Zhang, L.; Leng, X.; Walter, M. D.; Huang, Z. *J. Am. Chem. Soc.* **2013**, *135*, 19154−19166.
(45) Nishida, Y.; Kino, K.; Kida, S. *J. Chem. Soc., Dalton Trans.* **1987**, 1157−1161.
(46) Oliver, J. D.; Mullica, D. F.; Hutchinson, B. B.; Milligan, W. O. *Inorg. Chem.* **1980**, *19*, 165−169.
(47) Evans, D. F. *J. Chem. Soc.* **1959**, 2003−2005.
(48) Gütlich, P.; Ensling, J. *Mössbauer Spectroscopy in Inorganic Electronic Structure and Spectroscopy;* Solomon, E. I., Lever, A. B. P., Eds.;Wiley: New York, 2006; Vol. *I*.
(49) Brant, P.; Feltham, R. D. *J. Electron Spectrosc. Relat. Phenom.* **1983**, *32*, 205−221.
(50) Feltham, R. D.; Brant, P. *J. Am. Chem. Soc.* **1982**, *104*, 641−645.
(51) Brant, P.; Feltham, R. D. *Inorg. Chem.* **1980**, *19*, 2673−2676.
(52) Enemark, J. H.; Feltham, R. D. *Coord. Chem. Rev.* **1974**, *13*, 339−406.
(53) Cahen, D.; Lester, J. E. *Chem. Phys. Lett.* **1973**, *18*, 108−111.
(54) Moddeman, W. E.; Blackburn, J. R.; Kumar, G.; Morgan, K. A.; Albridge, R. G.; Jones, M. M. *Inorg. Chem.* **1972**, *11*, 1715−1717.
(55) Hu, L.; Liu, W.; Li, C.-H.; Zhou, X.-H.; Zuo, J.-L. *Eur. J. Inorg. Chem.* **2013**, *2013*, 6037−6048.
(56) Nielson, A. J.; Metson, J. B. *Polyhedron* **2012**, *31*, 143−149.
(57) Karpov, A.; Konuma, M.; Jansen, M. *Chem. Commun.* **2006**, 838−840.
(58) Langer, R.; Leitus, G.; Ben-David, Y.; Milstein, D. *Angew. Chem., Int. Ed.* **2011**, *50*, 2120−2124.
(59) Pelczar, E. M.; Emge, T. J.; Krogh-Jespersen, K.; Goldman, A. S. *Organometallics* **2008**, *27*, 5759−5767.
(60) Myers, T. W.; Berben, L. A. *Inorg. Chem.* **2012**, *51*, 1480−1488.
(61) Hong, S.; Huber, S. M.; Gagliardi, L.; Cramer, C. C.; Tolman, W. B. *J. Am. Chem. Soc.* **2007**, *129*, 14190−14192.
(62) Bianchini, C.; Mantovani, G.; Meli, A.; Migliacci, F.; Laschi, F. *Organometallics* **2003**, *22*, 2545−2547.
(63) Takaoka, A.; Peters, J. C. *Inorg. Chem.* **2011**, *51*, 16−18.
(64) De Bruin, B.; Hetterscheid, D. G. H.; Koekkoek, A. J. J.; Grützmacher, H. The Organometallic Chemistry of Rh-, Ir-, Pd-, and Pt-Based Radicals: Higher Valent Species. In *Progress in Inorganic Chemistry;* John Wiley & Sons, Inc., 2008; pp 247−354.
(65) Kannan, S.; Moody, M. A.; Barnes, C. L.; Duval, P. B. *Inorg. Chem.* **2006**, *45*, 9206−9212.
(66) Reger, D. L.; Watson, R. P.; Gardinier, J. R.; Smith, M. D.; Pellechia, P. J. *Inorg. Chem.* **2006**, *45*, 10088−10097.
(67) Gorelsky, S. I.; Ghosh, S.; Solomon, E. I. *J. Am. Chem. Soc.* **2006**, *128*, 278−290.

DOI: 10.1021/acs.inorgchem.5b00509
Inorg. Chem. 2015, 54, 4909−4926

(68) Zell, T.; Langer, R.; Iron, M. A.; Konstantinovski, L.; Shimon, L. J. W.; Diskin-Posner, Y.; Leitus, G.; Balaraman, E.; Ben-David, Y.; Milstein, D. *Inorg. Chem.* **2013**, *52*, 9636−9649.
(69) Note that a crucial influence on the ^{15}N chemical shift of the pyridine nitrogen atom is observed upon dearomatization of $[Fe(L_{PNN\text{-}bp})_2]^{2+}$ complexes (see ref 68).
(70) Fulmer, G. R.; Miller, A. J. M.; Sherden, N. H.; Gottlieb, H. E.; Nudelman, A.; Stoltz, B. M.; Bercaw, J. E.; Goldberg, K. I. *Organometallics* **2010**, *29*, 2176−2179.
(71) Marcó, A.; Compañó, R.; Rubio, R.; Casals, I. *Microchim. Acta* **2003**, *142*, 13−19.
(72) Lagaditis, P. O.; Sues, P. E.; Sonnenberg, J. F.; Wan, K. Y.; Lough, A. J.; Morris, R. H. *J. Am. Chem. Soc.* **2014**, *136*, 1367−1380.
(73) Bain, G. A.; Berry, J. F. *J. Chem. Educ.* **2008**, *85*, 532.
(74) Beamson, G.; Briggs, D. *High-Resolution XPS of Organic Polymers: The Scienta ESCA 300 Database;* Wiley: Chichester, U.K., 1992.
(75) Neese, F.; Solomon, E. I. *Inorg. Chem.* **1999**, *38*, 1847−1865.
(76) Pavel, E. G.; Kitajima, N.; Solomon, E. I. *J. Am. Chem. Soc.* **1998**, *120*, 3949−3962.
(77) Frisch, M. J.; Trucks, G. W.; Schlegel, H. B.; Scuseria, G. E.; Robb, M. A.; Cheeseman, J. R.; Scalmani, G.; Barone, V.; Mennucci, B.; Petersson, G. A.; Nakatsuji, H.; Caricato, M.; Li, X.; Hratchian, H. P.; Izmaylov, A. F.; Bloino, J.; Zheng, G.; Sonnenberg, J. L.; Hada, M.; Ehara, M.; Toyota, K.; Fukuda, R.; Hasegawa, J.; Ishida, M.; Nakajima, T.; Honda, Y.; Kitao, O.; Nakai, H.; Vreven, T.; Montgomery, J. A., Jr.; Peralta, J. E.; Ogliaro, F.; Bearpark, M.; Heyd, J. J.; Brothers, E.; Kudin, K. N.; Staroverov, V. N.; Kobayashi, R.; Normand, J.; Raghavachari, K.; Rendell, A.; Burant, J. C.; Iyengar, S. S.; Tomasi, J.; Cossi, M.; Rega, N.; Millam, M. J.; Klene, M.; Knox, J. E.; Cross, J. B.; Bakken, V.; Adamo, C.; Jaramillo, J.; Gomperts, R.; Stratmann, R. E.; Yazyev, O.; Austin, A. J.; Cammi, R.; Pomelli, C.; Ochterski, J. W.; Martin, R. L.; Morokuma, K.; Zakrzewski, V. G.; Voth, G. A.; Salvador, P.; Dannenberg, J. J.; Dapprich, S.; Daniels, A. D.; Farkas, Ö.; Foresman, J. B.; Ortiz, J. V.; Cioslowski, J.; Fox, D. J. *Gaussian 09,* Revision D.01; Gaussian, Inc.: Wallingford, CT, 2013.
(78) Schäfer, A.; Huber, C.; Ahlrichs, R. *J. Chem. Phys.* **1994**, *100*, 5829−5835.
(79) Tomasi, J.; Mennucci, B.; Cammi, R. *Chem. Rev.* **2005**, *105*, 2999−3094.
(80) Gorelsky, S. I. *AOMix: Program for Molecular Orbital Analysis.* http://www.sg-chem.net/, version 6.85, 2014.
(81) Gorelsky, S. I.; Lever, A. B. P. *J. Organomet. Chem.* **2001**, *635*, 187−196.
(82) Zeng, X.; Coquière, D.; Alenda, A.; Garrier, E.; Prangé, T.; Li, Y.; Reinaud, O.; Jabin, I. *Chem.—Eur. J.* **2006**, *12*, 6393−6402.
(83) Zhang, W.; Liu, J.; Zhu, H.; Gao, W.; Sun, L. *Synth. Commun.* **2007**, *37*, 3393−3402.

DOI: 10.1021/acs.inorgchem.5b00509
Inorg. Chem. 2015, 54, 4909−4926